RESEARCH ARTICLE SUMMARY

MOLECULAR BIOLOGY

ATP-dependent remodeling of chromatin condensates reveals distinct mesoscale outcomes

Camille Moore, Emily Wong, Upneet Kaur, Un Seng Chio, Ziling Zhou, Megan Ostrowski, Ke Wu, Iryna Irkliyenko, Sean Wang, Vijay Ramani*, Geeta J. Narlikar*

Full article and list of author affiliations: https://doi.org/10.1126/science.adr0018

INTRODUCTION: Adenosine triphosphate (ATP)–dependent chromatin remodelers can slide, disassemble, deform, and space nucleosomes. However, each remodeler has a distinct impact on nucleosomes. For example, the imitation switch remodeler ACF has been shown to generate the evenly spaced nucleosome architecture found in heterochromatin. By contrast, the switch/sucrose nonfermentable remodeler RSC slides, deforms, and disassembles nucleosomes and is critical for enabling DNA access in euchromatin. Most of our mechanistic understanding of remodeler action derives from detailed studies at the nucleosome scale. At the genomic scale, studies have shown correlations between specific remodelers and changes in chromatin organization in cells. However, whether and how the action of chromatin remodelers at the nucleosome scale affects chromatin dynamics at the mesoscale remains an open question.

RATIONALE: In cells, remodelers must operate within a crowded chromatin environment with estimated nucleosome concentrations of ~100 μM or higher. How chromatin remodelers act in such a crowded environment is poorly understood. A simple prediction is that ATP-driven nucleosome mobilization disrupts interactions between nucleosomes, resulting in local chromatin decondensation. Thus, remodelers may act as molecular "stir bars." Previous work has shown that chromatin compacts into phase-separated condensates in vitro. These condensates have nucleosome concentrations comparable to those within the nucleus. We build on these studies to ask how two key remodelers ACF and RSC—which carry out substantially different transformations of a nucleosome—contend with a crowded chromatin environment. Further, as chromatin varies in nucleosome density and spacing in cells, we also investigate how nucleosome spacing and density affect chromatin condensation.

RESULTS: To investigate the interplay between condensed chromatin and remodelers, we reconstituted chromatin in vitro on a genomic DNA sequence and combined confocal imaging of chromatin condensates with single-molecule footprinting of chromatin fibers. We found that increasing the density of nucleosomes promoted phase separation after controlling for total nucleosome concentration, consistent with increased nucleosomal valency promoting chromatin condensation. The condensates were also highly viscous. However, despite the high viscosity of the chromatin condensates, ACF and RSC could still remodel nucleosomes within this environment and each remodeler generated similar products as observed previously with uncondensed chromatin. Remodeling by ACF does not substantially affect chromatin condensation whereas remodeling by RSC decondenses the chromatin. RSC-mediated nucleosome occlusion and RSC-remodeled chromatin products both drive chromatin decondensation. The extent of the occlusion effect depends on the molar ratio of RSC:nucleosome. Furthermore, RSC activity promotes micron-scale motions of entire condensates, unlike ACF. This additional RSC activity may reduce the local chromatin viscosity and enable faster diffusion of transcriptional factors in cells.

CONCLUSION: Our findings demonstrate that ATP-dependent remodelers do not generically act as molecular stir bars; rather, their mesoscale effects on chromatin derive from their specific, nucleosome-scale interactions and activities. The biological importance of remodelers may thus reflect both their effects on nucleosome mobilization and the corresponding consequences on chromatin dynamics at the mesoscale. Future work is needed to clarify whether other nucleosome remodelers that catalyze distinct transformations of nucleosomes also have distinct effects on meso-scale chromatin dynamics. □

*Corresponding author. Email: vijay.ramani@gladstone.ucsf.edu and geeta.narlikar@ucsf.edu Cite this article as Camille Moore *et al.*, *Science* **390**, eadr0018 (2025). DOI: 10.1126/science.adr0018

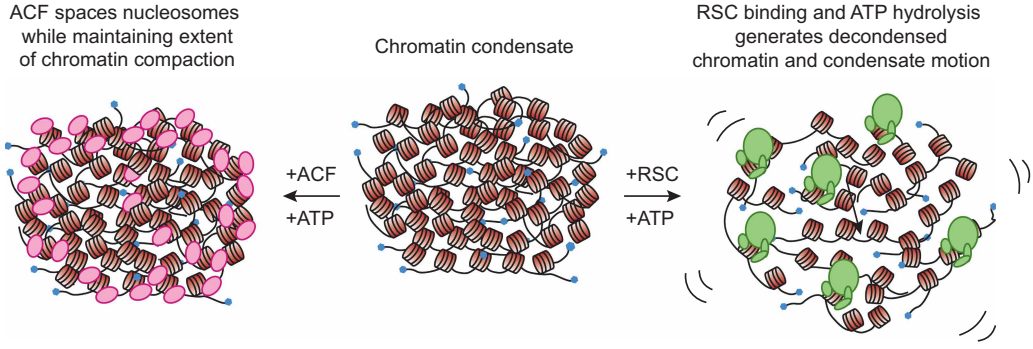

Effects of ATP-dependent chromatin remodelers on mesoscale chromatin organization and dynamics in vitro. Both ACF and RSC can remodel nucleosomes within chromatin condensates. Remodeling by ACF does not substantially affect chromatin condensation whereas remodeling by RSC decondenses chromatin. RSC-mediated nucleosome occlusion and RSC-remodeled chromatin products both drive chromatin decondensation.

MOLECULAR BIOLOGY

ATP-dependent remodeling of chromatin condensates reveals distinct mesoscale outcomes

Camille Moore[1,2,3], Emily Wong[1]†, Upneet Kaur[1]†, Un Seng Chio[1], Ziling Zhou[1], Megan Ostrowski[3], Ke Wu[3], Iryna Irkliyenko[3], Sean Wang[3], Vijay Ramani[1,3]*, Geeta J. Narlikar[1]*

Adenosine triphosphate (ATP)–dependent chromatin remodeling enzymes mobilize nucleosomes, but how such mobilization affects chromatin condensation is unclear. We investigate effects of two major remodelers, ACF and RSC, using chromatin condensates and single-molecule footprinting. We find that both remodelers inhibit the formation of condensed chromatin. However, the remodelers have distinct effects on preformed chromatin condensates. ACF spaces nucleosomes without decondensing the chromatin, explaining how ACF maintains nucleosome organization in transcriptionally repressed genomic regions. By contrast, RSC catalyzes ATP-dependent decondensation of chromatin. RSC also drives micron-scale movements of entire chromatin condensates. These additional activities of RSC may contribute to its central role in transcription. The biological importance of remodelers may thus reflect both their effects on nucleosome mobilization and the corresponding consequences on chromatin dynamics at the mesoscale.

Chromatin condensation typically correlates with transcription repression, such that transcriptionally repressed heterochromatin is more condensed than transcriptionally active euchromatin (*1*, *2*). Adenosine triphosphate (ATP)–dependent chromatin remodelers play critical roles in the formation and maintenance of these distinct chromatin domains (*3*–*5*) by acting on nucleosomes, which consist of ~140 base pairs (bp) of DNA wrapped around an octamer of histone proteins (*6*).

Remodelers can slide, disassemble, deform, and space nucleosomes but each remodeler has a distinct impact on nucleosomes (*3*, *4*). For example, the imitation switch (ISWI) class remodeler ACF has been shown to generate the evenly spaced nucleosome architecture found in heterochromatin (*7*–*11*). In comparison, the switch/sucrose nonfermentable (SWI/SNF) class remodeler RSC—which slides, deforms, and disassembles nucleosomes—is critical for enabling DNA access in euchromatin (*12*–*15*). Most of our mechanistic understanding of remodeler action derives from studies at the nucleosome scale. At the genomic scale, chromatin immunoprecipitation–based and genetic studies have shown correlations between the presence of specific remodelers and changes in chromatin organization in cells, and in vitro Micro-C studies have suggested that remodeler-driven nucleosome positions may promote formation of chromatin domains (*16*–*20*). However, how remodeler action at the nucleosome scale affects chromatin dynamics at the mesoscale remains an open question.

One simple prediction is that ATP-driven nucleosome mobilization disrupts interactions between nucleosomes, resulting in local chromatin decondensation. Thus, remodelers may act as molecular "stir bars" (*21*). Additionally, in cells, remodelers must operate within a crowded chromatin environment with estimated nucleosome concentrations of ~100 μM or higher (*22*). How chromatin remodelers act in such a crowded environment is poorly understood. Recent studies have shown that chromatin condenses into phase-separated droplets in vitro that have nucleosome concentrations comparable to those within the nucleus (*23*, *24*). We build on these studies to ask how two key remodelers, ACF and RSC, which carry out substantially different transformations of a nucleosome, contend with a crowded chromatin environment. Further, as chromatin varies in nucleosome density and spacing in cells, we also investigate how nucleosome spacing and density affect chromatin condensation.

To investigate the interplay between condensed chromatin and remodelers, we combined single-molecule footprinting of chromatin fibers reconstituted in vitro on a native DNA sequence [single-molecule adenine methylated oligonucleosome sequencing assay of chromatin accessibility on assembled templates (SAMOSA-ChAAT)] (*25*) with confocal imaging of chromatin condensates. We found that despite the high viscosity of the chromatin condensates, ACF and RSC could still act on nucleosomes within this environment. In contrast to simple predictions, ACF remodeling did not decondense chromatin, but RSC remodeling did. Additionally, unlike ACF, RSC activity promoted micron-scale motions of entire condensates. Our findings demonstrate how remodeling activities that differ at the nucleosome scale can differentially change the chromatin environment at the mesoscale.

Nucleosome density regulates chromatin condensation

Previous studies have shown that chromatin assembled on DNA containing evenly spaced artificial 601 nucleosome positioning sequences forms phase-separated condensates under physiologically relevant buffer conditions (*23*, *24*, *26*). To investigate the phase separation properties of chromatin assembled on a native sequence with less nucleosome positioning capability, we assembled chromatin on a 3.2-kb DNA sequence from the 5′ end of mouse gene *Cyp3a11* [sequence "S3", in relation to sequences S1 and S2 studied previously (*25*)]. Chromatin was assembled on fluorescently end-labeled S3 and imaged by confocal microscopy under physiologically relevant buffer conditions (75 to 150 mM KCl, 1.5 mM free Mg^{2+}) (Fig. 1A) (*27*). Single-molecule nucleosome positions were determined using SAMOSA-ChAAT (*25*, *28*). In contrast to chromatin assembled on templates with evenly spaced 601 sequences, chromatin assembled on S3 had irregular nucleosome positions, consistent with observations for nucleosomes assembled on other physiological sequences (*25*, *28*).

Chromatin condensates are formed and stabilized by internucleosomal interactions between fibers (*23*). Thus, an increased number of nucleosomes per DNA template is expected to promote condensation. Indeed, previous studies have shown that when nucleosome density is kept constant using evenly spaced 601 sequences, shorter nucleosome arrays with 4 or 6 nucleosomes phase-separate more poorly than longer arrays with 12 nucleosomes (*23*). We built on this finding by varying nucleosome density while keeping the DNA length constant. We found that increasing the density of nucleosomes promoted phase separation even after controlling for total nucleosome concentration (Fig. 1B and fig. S1). Furthermore, the distribution of linker lengths between nucleosomes could not explain the differences in chromatin condensation (fig. S2). Consistent with previous studies using the 12×601 array system, we found that deleting the H4 tail inhibited condensate formation whereas mutating the acidic patch formed by H2A and H2B did not have a large impact on condensation (*23*) (fig. S7). We therefore attribute the increased condensation with increased nucleosome density to a higher valency arising from a larger number of nucleosomes per DNA molecule.

In every assembly, we observed a distribution of nucleosomes per DNA template (Fig. 1, C and D, and fig. S3), as previously observed (*25*). The median of this distribution shifted depending on how much histone octamer was used. Using the nucleosome density and the DNA concentration in the condensates, we calculated the concentration of

[1]Department of Biochemistry and Biophysics, University of California, San Francisco, San Francisco, CA, USA. [2]Tetrad Graduate Program, University of California, San Francisco, San Francisco, CA, USA. [3]Gladstone Institute for Data Science & Biotechnology, San Francisco, CA, USA. ***Corresponding author. Email: vijay.ramani@gladstone.ucsf.edu (V.R.); geeta.narlikar@ucsf.edu (G.J.N.)** †These authors contributed equally to this work.

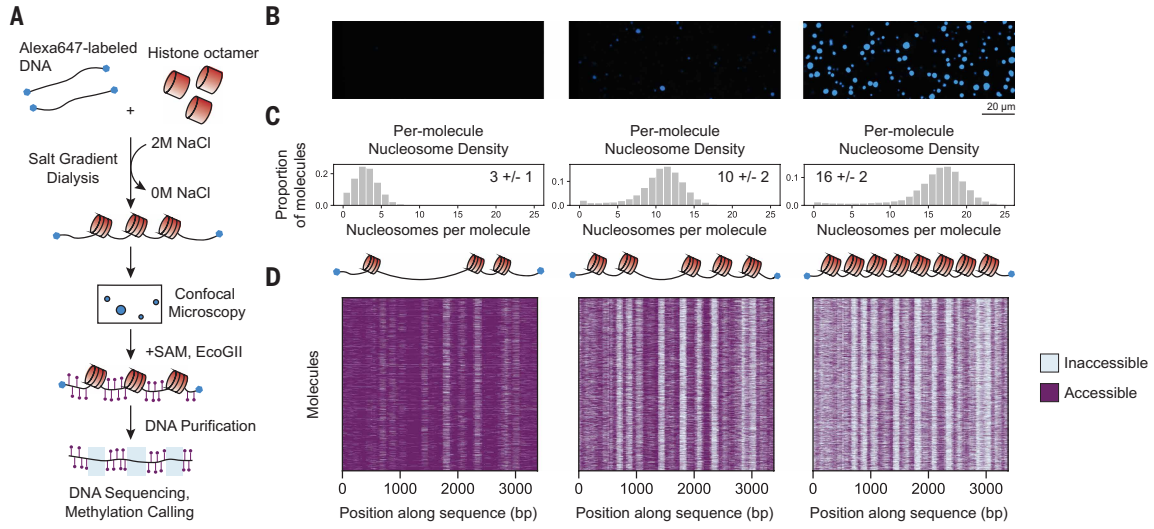

Fig. 1. Nucleosome density affects chromatin condensate formation. (**A**) Scheme of experimental workflow. (**B**) Confocal images of chromatin reactions with varying histone octamer concentration showing Alexa647 fluorescence. (**C**) Nucleosomes per chromatin molecule for each chromatin assembly shown in (B). Inset numbers on plots are median nucleosomes per molecule and median absolute deviation. (**D**) Heatmaps of accessible and inaccessible bases for 3000 molecules per condition. Illustrated chromatin molecules show that each row in the heatmap represents a chromatin molecule and that the number of nucleosomes per molecule increases according to octamer concentration.

nucleosomes in the medium and high-density chromatin condensates to be 7.6 ± 4 μM and 40 ± 23.5 μM, respectively (fig. S1, D and F, and Materials and methods). The nucleosome concentration in the high-density chromatin is comparable to concentrations measured by other groups (*23*) and to that estimated within the nucleus (*22*). Each chromatin assembly also likely contained a small fraction of hexasomes and tetrasomes.

We next investigated the dynamics of chromatin within the condensates by measuring the fluorescence recovery after photobleaching (FRAP). Regularly spaced nucleosome arrays assembled on comparably long DNA templates containing 601 repeats (2 kb to 3.3 kb) have been shown to display substantial FRAP within 10 min, a feature we also recapitulated (fig. S4) (*26*). By contrast, we saw minimal fluorescence recovery within the S3 condensates 10 min after photobleaching under all conditions, including a condition tested previously for the evenly spaced 601 arrays (figs. S1C and S4B) (*26*). As a complementary assay for chromatin dynamics, we performed a droplet mixing experiment using chromatin that was end-labeled with either AlexaFluor647 or AlexaFluor555. Upon mixing, we observed distinct, single-colored chromatin territories, indicating that these droplets were viscous, with low internal mixing (fig. S1E). However, the merged droplets were spherical, indicating that fused chromatin condensates do coalesce to minimize surface tension. Overall, our results suggest that condensates formed from a homogenous mixture of uniformly spaced nucleosomes on Widom 601 repeats have different biophysical properties compared with our condensates, which were formed from a heterogeneous mixture of irregularly spaced nucleosomes on a specific genomic sequence. These differences may arise from differences in interarray interactions inside the chromatin condensates.

Given the high viscosity of the condensates, we wondered whether chromatin remodelers could access their nucleosomal substrates. We therefore investigated how the addition of remodeler affected (i) the formation of chromatin condensates and (ii) the properties of preformed chromatin condensates. In both cases, we concomitantly assayed remodeling activity using SAMOSA-ChAAT.

ACF inhibits formation of chromatin condensates in an ATP-independent manner

ACF generates regular chromatin arrays in vivo and in vitro and catalyzes nucleosome spacing by sensing flanking DNA lengths (*25*, *29*). To investigate how ACF regulates chromatin condensation, we mixed ACF with chromatin containing a median of 19 nucleosomes per template (Fig. 2, A to C). In the presence of ATP, ACF spaced nucleosomes in a nucleosome density–dependent manner. The distance between nucleosomes was regular for a given DNA molecule but varied from molecule to molecule depending on nucleosome density (Fig. 2B and fig. S5). This observation is consistent with our previous work demonstrating density-dependent spacing by ACF on different genomic templates (*25*). Nucleosome footprints in reactions with ADP did not change relative to control chromatin (fig. S6A).

ACF inhibited the formation of chromatin condensates, and condensates that did form were less intense and more irregularly shaped (Fig. 2B). ACF had a similar effect in the presence of ADP or ATP, suggesting that binding by ACF to the arrays—rather than its nucleosome spacing activity—was responsible for inhibiting condensation and altering condensate morphology (fig. S6). Consistent with a binding effect, ACF inhibited chromatin condensation in a concentration-dependent manner, showing increased inhibition at higher molar ratios of ACF to nucleosomes (Fig. 2B). These results rule out the model in which ATP-driven nucleosome mobilization by ACF prevents chromatin condensation. Rather, the data suggest that ACF binding occludes the nucleosomal surfaces that participate in internucleosomal interactions. It has previously been shown that mutating the acidic patch impairs binding by SNF2h, the catalytic subunit of ACF (*30*). Therefore, to further test our binding-based model, we assembled chromatin using acidic patch mutant (APM) histone octamers (fig. S7). We found that ACF inhibited condensation of APM chromatin substantially less than wild-type (WT) chromatin and did not affect the morphology of these condensates (fig. S8). These results are consistent with the model in which ACF inhibits chromatin condensation by binding and occluding nucleosomal surfaces.

Chromatin remodeled by ACF does not show a large increase in compaction within condensates

Nucleosome spacing has been shown to affect chromatin condensation (*23*), raising the question of whether the evenly spaced chromatin generated by ACF would change compaction within condensates compared with the irregularly spaced chromatin. To address this question, we depleted ACF from chromatin after remodeling using magnetic anti-FLAG beads (Fig. 2D and fig. S9). We found that two sequential

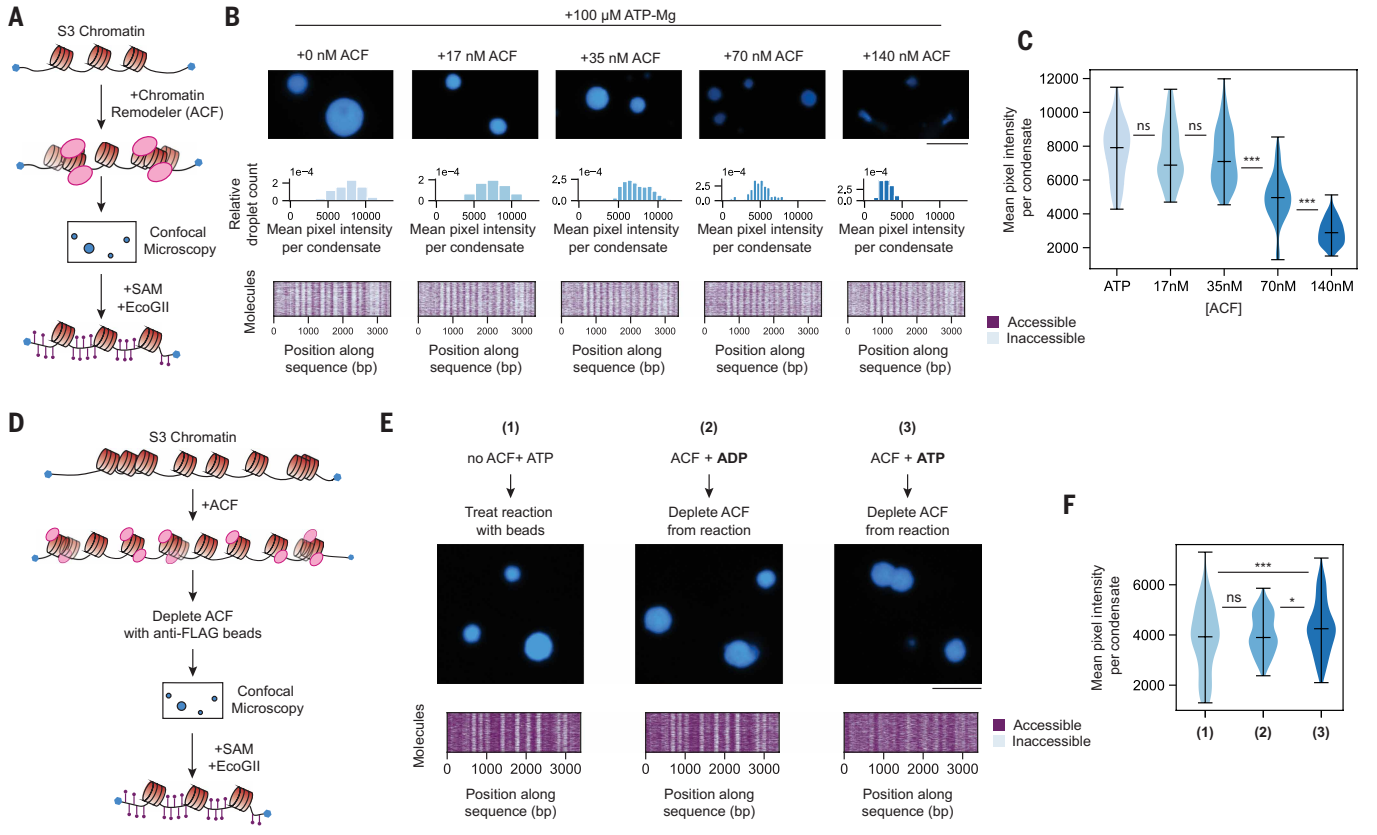

Fig. 2. Effects of ACF activity and ACF-induced nucleosome spacing on chromatin condensation. (**A**) Scheme of premix experimental workflow. (**B**) Titration of ACF in the presence of ATP-Mg in reactions with a 20 nM chromatin array and 380 nM nucleosome. Confocal images show Alexa647 fluorescence. Histograms of mean pixel intensity per condensate with histogram bin number equal to 0.1 × number of condensates per condition. Heatmaps show accessible and inaccessible bases for 1000 molecules per condition. (**C**) Violin plot of mean pixel intensity per condensate for condensates in conditions from (B). (Left to right) 93, 88, 200, 283, and 181 condensates were selected. (**D**) Scheme of ACF depletion experimental workflow. (**E**) Confocal images of condensates after anti-FLAG beads depletion. Heatmaps show accessible and inaccessible bases for 1000 molecules per condition. (**F**) Violin plot of mean pixel intensity per condensate for condensates in conditions from (E). (Left to right) 195, 133, and 183 condensates were selected. All scale bars are 5 μm.

incubations with the anti-FLAG beads with 300 mM salt was optimal for ACF depletion, resulting in at least a 34-fold reduction in ACF (fig. S9). These condensates formed from ACF remodeled chromatin and after ACF depletion were only subtly denser than those formed from unremodeled chromatin (Fig. 2, E and F). We saw similar results using chromatin assembled on another genomic sequence S1 (fig. S10). Based on these results, we concluded that the nucleosome spacing generated by ACF only subtly increases chromatin density inside condensates.

ACF remodels nucleosomes in preformed condensates without dissolving them

Given our observation that ACF inhibited formation of chromatin condensates in a concentration-dependent manner, we wondered whether ACF would also dissolve preformed chromatin condensates. To test this possibility, we added ACF to preformed chromatin condensates (Fig. 3A). Chromatin condensates persisted after adding ACF, regardless of whether we added 350 nM or 800 nM ACF to condensates generated from chromatin with ~300 nM nucleosomes (Fig. 3B and fig. S5C). These findings contrast with those in Fig. 2, showing that premixing 140 nM ACF with chromatin inhibited condensate formation. We hypothesized that only a minimal amount of ACF entered the preformed condensates.

To quantify the amount of the ACF within the condensates, we fluorescently labeled ACF and repeated the add-in reaction using condensates generated from arrays with 300 nM nucleosome and 350 nM ACF. We observed ACF throughout the condensates, but it was not evenly distributed (Fig. 3E and fig. S11E). ACF was approximately two times as concentrated (~6 μM) on the surfaces of the chromatin condensates compared with the interior of the condensates (~3 μM). Based on the mean nucleosome concentration within these condensates of ~71 μM, we calculated the ratio of ACF:nucleosome inside the condensates as maximally 1:12 and minimally 1:24. This explained why ACF did not solvate the preformed condensates, because in our previous experiments ACF detectably inhibited chromatin condensation when the ACF:nucleosome molar ratio was at 1:3 or higher. The decreasing concentration gradient of ACF toward the center of the condensates suggested that ACF was diffusing slowly throughout the condensates. To assay ACF dynamics within the condensates, we FRAPed the labeled ACF. We observed no detectable FRAP at the edge or interior of the condensates over the course of 5 min (Fig. 3F). Notably, the photobleached spots, ~1 μm in diameter, contained tens of thousands of nucleosomes. Thus the slow recovery does not necessarily imply that ACF was indefinitely stuck on nucleosomes, but rather that it diffused slower than the order of several minutes across micron-scale distances and through this nucleosome environment. The arrays in these reactions were completely remodeled by ACF at 2 hours (Fig. 3C and fig. S5), indicating that over time, even substochiometric ACF was able to access and remodel all the nucleosomes (fig. S5).

The slow diffusion of ACF through the condensate was not ATP-dependent, as even in the presence of ADP we observed enrichment of ACF at the periphery of the condensates (fig. S11E). Therefore, we hypothesized that the nM-order K_d of ACF for nucleosomes

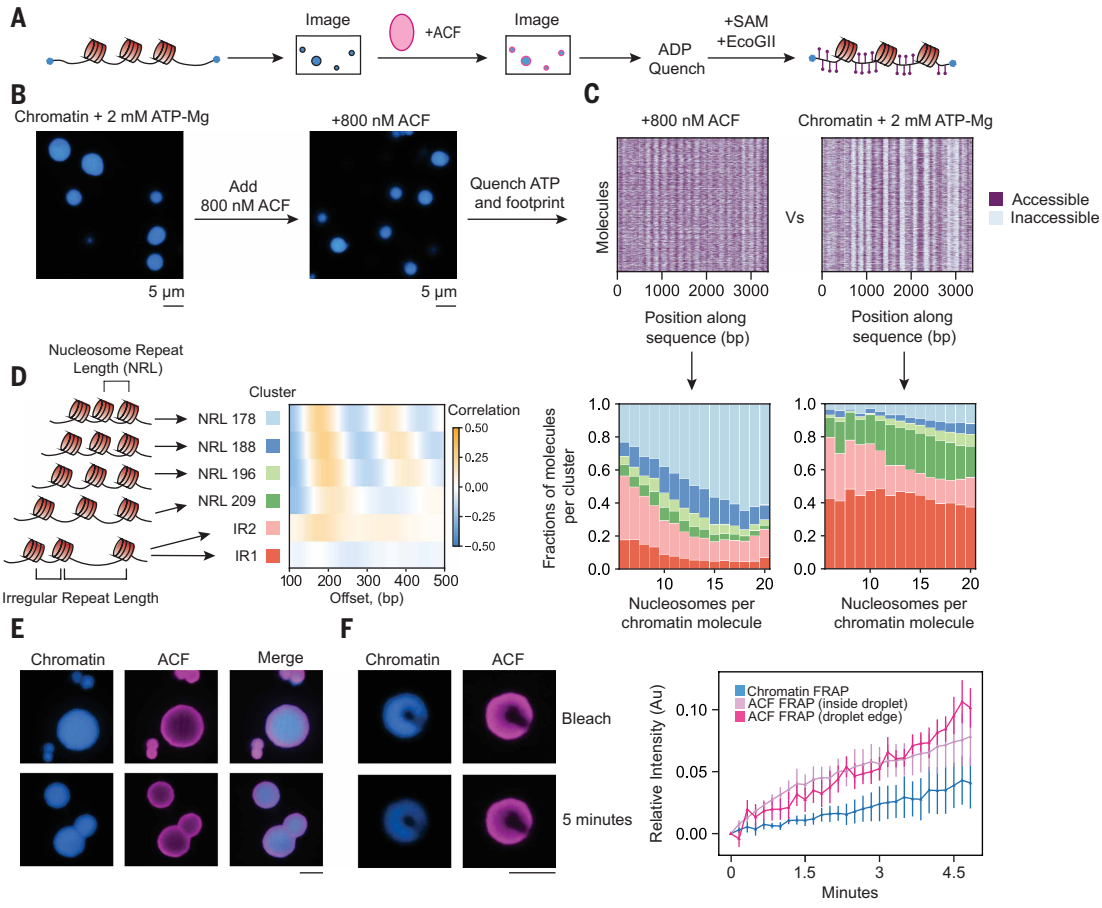

Fig. 3. ACF remodels chromatin inside of condensates and is concentrated in condensates. (**A**) Scheme of ACF add-in experimental workflow. (**B**) Example condensates before and after adding in ACF. Chromatin is labeled with AF647 and was initially added at 20 nM with 320 nM nucleosome. (**C**) Heatmaps of accessible and inaccessible bases for 3000 molecules from the add-in reaction and control reaction. (**D**) (Left) Average single-molecule autocorrelograms resulting from Leiden clustering of individual molecules. We observe six different array types, four with regular spacing [nucleosome repeat length (NRL)] and two with irregular spacing (IR). (Right) Stacked bar chart representation of cluster representation for chromatin molecules from two different conditions, plotted as a function of nucleosome density. In the presence of ACF and ATP, the proportion of evenly spaced fibers (green and blue colors) increases and the proportion of irregularly spaced fibers (pink and red colors) decreases. (**E**) Example condensates after adding ACF using AF488-labeled ACF. Chromatin is labeled with AF647 and was initially added at 20 nM, with 300 nM nucleosome. (**F**) Example droplet before and after photobleaching, AF647 and AF488 channels. Quantification of recovery after photobleaching for chromatin (AF647), $n = 8$ condensates and ACF (AF488), $n = 8$ condensates for internal and $n = 5$ condensates for external. Recovery is normalized to pre-bleach droplet intensity and unbleached droplets over the time course. All scale bars are 5 μm.

contributed to its slow diffusion through chromatin (*29*, *31*). Consistent with this possibility, single-molecule Förster resonance energy transfer data have shown that ACF processively remodels nucleosomes, with ATP-dependent residence times of 5 min or longer on individual mononucleosomes (*32*). If high affinity and processivity were responsible for the slow diffusion of ACF through chromatin, then a less processive remodeler with a lower affinity for nucleosomes may diffuse more quickly and uniformly. We therefore repeated the experiment with Snf2h, the catalytic subunit of ACF, which is less processive and has a ~50-fold weaker affinity for nucleosomes than ACF (*29*, *31*, *33*). Consistent with our hypothesis, labeled Snf2h recovered from photobleaching much faster (within 1 min) and uniformly distributed throughout chromatin condensates in the presence of ATP or ADP (fig. S11, C and D). In congruence with this result, previous studies show that the catalytic subunit of *Drosophila* ISWI complexes, which has a lower affinity for nucleosomes than ACF, diffuses rapidly and uniformly through chromatin condensates within minutes, though only in the presence of ATP (*34*).

Because ACF generates chromatin fibers with regularly spaced nucleosomes, we hypothesized that ACF-remodeled products would display more rapid dynamics within the condensates, similar to the evenly spaced 12 × 601 arrays. However, we observed no FRAP recovery over 5 min for chromatin remodeled by ACF (Fig. 3F). Depleting ACF also did not increase FRAP (fig. S9C). One possible explanation for this result is that even if all nucleosomes are evenly spaced by ACF, the nucleosome spacing varies from molecule to molecule as some chromatin molecules have more nucleosomes than others. The spacing distributions are best illustrated in the single-turnover ACF samples (fig. S5B; 800 nM ACF). By contrast, essentially all of the regularly spaced 12×601 array molecules have the same nucleosome spacing as a result of the strength of this positioning sequence (*28*). It is therefore possible that uniform spacing across all chromatin molecules within a condensate increases dynamics.

RSC uses ATP to decondense chromatin and mobilize whole condensates

In contrast to ACF, RSC generates a wider variety of nucleosomal products, so we next investigated whether the different outcomes on nucleosomes would result in different outcomes within condensates. We first analyzed how RSC remodeling affected the formation of chromatin condensates by premixing RSC with chromatin containing a median of 15 nucleosomes per template (Fig. 4A). In the presence of 100 μM ATP-Mg, we observed that RSC addition resulted in condensates that

were smaller and less intense than in the control (Fig. 4, B and C; fig. S15B; and movies S1 to S4). However, RSC inhibited chromatin condensation substantially more in the presence of adenosine diphosphate (ADP) or adenylyl-imidodiphosphate (AMP-PNP) (Fig. 4, B and C). These results suggested that analogous to ACF, binding by RSC concealed the nucleosomal surfaces that participate in internucleosomal interactions when bound to ADP or AMP-PNP. RSC contacts the acidic patch formed by H2A and H2B, and RSC remodeling of mono-nucleosomes is impaired by mutation of basic residues in its catalytic subunit or by LANA peptide binding the acidic patch (*35*–*38*).

Consistent with the model in which RSC binding inhibits chromatin condensation, we found that RSC decondensed APM chromatin more modestly than WT chromatin (fig. S12).

At concentrations of ADP where RSC dissolved condensates, we saw a different effect with the same concentrations of RSC and ATP. Specifically, condensates were maintained, indicating that in the presence of ATP, RSC had effects on condensates beyond binding-based occlusion of nucleosomal surfaces.

Unlike ACF, the RSC complex slides, disassembles, and deforms nucleosomes without evenly spacing them (*5*, *12*, *39*). These activities

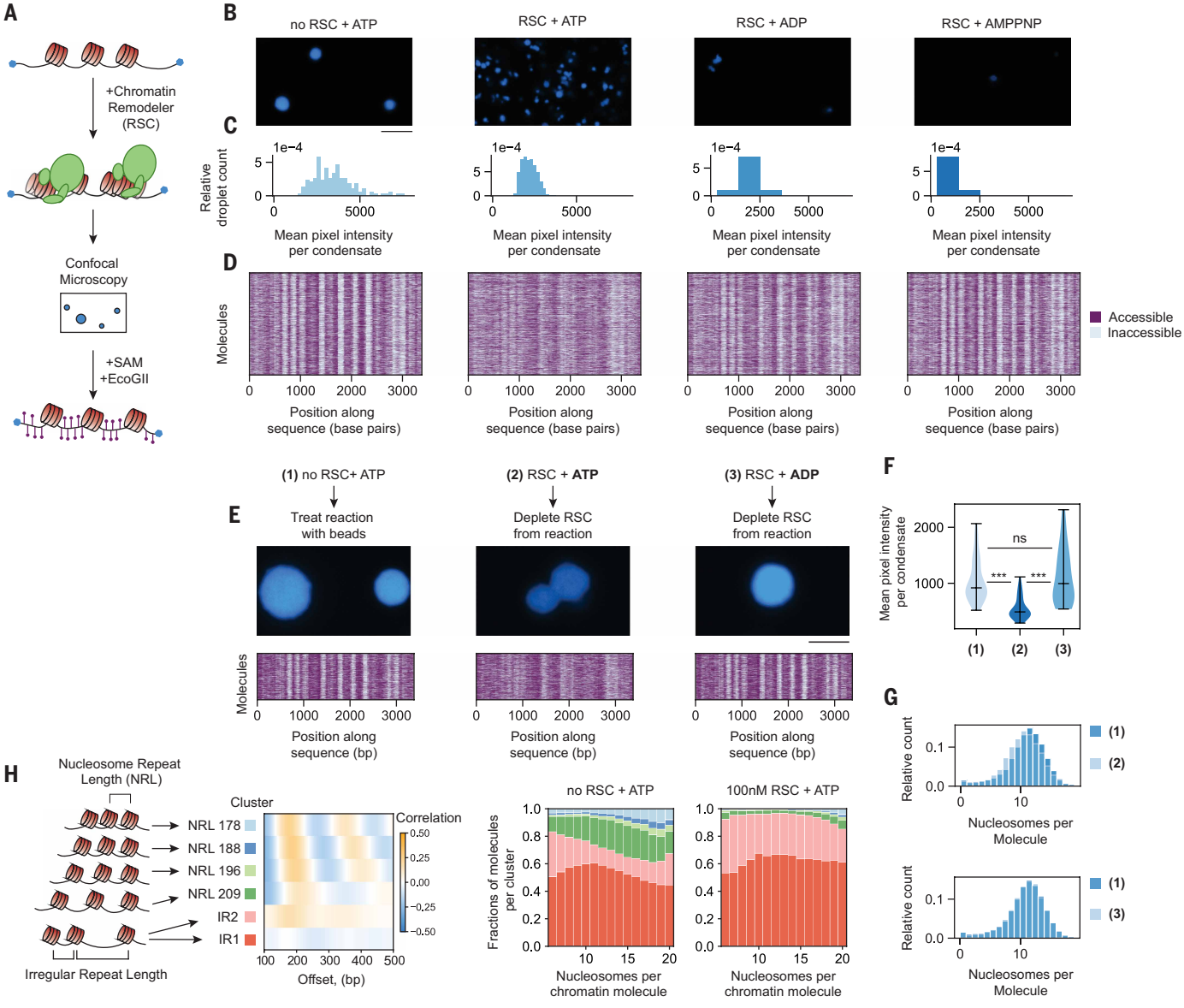

Fig. 4. RSC inhibits chromatin condensation and generates diverse nucleosome products that are not evenly spaced. (**A**) Scheme of premix experimental workflow. (**B**) RSC reactions have 100 nM RSC, 100 μM nucleotide-Mg^{2+}, and 220 nM nucleosome with median 15 nucleosomes per molecule. Confocal images show Alexa647 fluorescence; scale bar, 10 μm. (**C**) Histograms of mean pixel intensity per condensate, with bin size equal to 0.1 × number of condensates per condition. (**D**) Heatmaps of accessible and inaccessible bases for 2000 molecules per condition. (**E**) Confocal images and heatmaps of chromatin after RSC depletion (scheme outlined in Fig. 2D). Scale bar, 5 μm. (**F**) Violin plot of mean pixel intensity per condensates for conditions in (E). (Left to right) 65, 67, and 34 condensates were selected. (**G**) Histogram of nucleosomes per chromatin molecule for conditions in (E), 1000 molecules per condition. (**H**) (Left) Average single-molecule autocorrelograms resulting from Leiden clustering of individual molecules from (D). We observe six different array types, four with regular spacing (NRL) and two with irregular spacing (IR). (Right) Stacked bar chart representation of cluster representation for molecules from two different conditions, plotted as a function of nucleosome density. In the presence of RSC and ATP, the proportion of IR fibers (red and pink colors) increases.

are ATP-dependent, but RSC can also bind and distort nucleosomes without ATP (*12*, *40*). We observed that RSC substantially displaced nucleosome footprints from their original positions in the presence of ATP (Fig. 4D). We also observed minor footprint displacement in the context of ADP (Fig. 4D). By contrast, almost no displacement was seen with AMP-PNP (Fig. 4D). Not all nucleosomes were remodeled to the same extent with ATP, suggesting that the outcome of remodeling depends on DNA sequence (Fig. 4D) (*39*, *41*). Furthermore, the remodeled nucleosomes were not evenly spaced, as confirmed by autocorrelation analysis (Fig. 4H and fig. S13C). Overall, our analysis indicated that RSC catalyzed outcomes on S3 chromatin that are consistent with its previously characterized activities on nucleosomes (*5*, *12*, *14*, *39*).

We next determined whether the RSC-remodeled chromatin products contributed to the decreased chromatin condensation. We incubated RSC with chromatin in the presence of ATP or ADP, and after allowing for sufficient reaction time, we depleted RSC from these reactions and observed condensation of the chromatin (Fig. 4, E and F, and fig. S14). Depleting RSC from the ADP containing reactions enabled chromatin to form condensates with intensities similar to that of chromatin untreated with RSC. This result indicates that the effect of RSC on inhibiting condensation in the presence of ADP was due to RSC binding. By contrast, depleting RSC from the ATP reaction resulted in condensates with lower intensity compared with chromatin untreated with RSC. This result indicates that ATP-dependent remodeling by RSC generates chromatin that forms less dense condensates (Fig. 4, E and F, and fig. S14). We speculate that this effect is due to RSC-induced nucleosome positioning as well as increased populations of nucleosomes with distorted DNA, hexasomes, and tetrasomes.

We next tested how RSC interacted with preformed condensates. Adding RSC to preformed chromatin condensates in the presence of ATP made them larger and less intense (scheme shown in Fig. 5, A and B to F; movies S5 to S12; and fig. S15). The volume increase calculated for the condensates accounted for the lower nucleosome concentration (see Materials and methods) consistent with decondensation rather than loss of chromatin from the droplets. Further, the condensates were more mobile in the presence of RSC and ATP. To test whether this increased droplet motion required active ATP hydrolysis, we compared RSC action at 100 μM and 2 mM ATP. At both ATP concentrations, the chromatin is expected to be completely remodeled at the time of imaging (30 min). To assess condensate motion, we controlled for effects of droplet size on droplet motion by size-matching condensates, and quantified droplet motion focusing on the highest mobility droplets for each condition (Materials and methods; Fig. 5, E and F; fig. S15; and movies S5 to S12; see fig. S13G for distributions of condensate motion of all tracked condensates). First, we found that there was more condensate motion at the higher ATP concentration. Next, we repeated this experiment but let the condensates form for more time in the microscopy plate before initial imaging (18 hours versus 1.5 hours, in order to match condensate intensities between 100 μM and 2 mM ATP conditions). Upon adding RSC, we observed qualitatively similar results as in Fig. 5 (figs. S16 and S17). These results are consistent with a model in which condensate motion depends on active ATP hydrolysis by RSC.

The data above uncover some major differences between how ACF and RSC affect compacted chromatin. Unlike with ACF, RSC-mediated occlusion of nucleosomes and RSC-remodeled chromatin products both drive chromatin decondensation. The extent of the occlusion effect depends on the molar ratio of RSC:nucleosome. Furthermore, unlike ACF, RSC also increases condensate motion. To better understand how RSC may drive condensate motion, we investigated how RSC was distributed within the condensates. Unlike ACF, we found that RSC was evenly distributed throughout the condensates with ATP or ADP and recovered from photobleaching within 10 min (Fig. 5G and fig. S13, I to J). This finding is consistent with the lower residency time of RSC on nucleosomes compared with ACF in vitro (*42*). However, similar to ACF, we observed substoichiometric RSC relative to nucleosomes (1 RSC:13 nucleosomes) inside the condensates even when stoichiometric concentrations of RSC were added into the condensates.

Discussion

Nucleosome concentrations are estimated to range from ~100 to 500 μM in vivo (*22*), and how chromatin remodelers act within such crowded environments is poorly understood. Chromatin condensates allow recreation of comparably crowded conditions in vitro. By carrying out mechanistic biochemistry in chromatin condensates, we have uncovered new consequences of ATP-dependent chromatin remodeling by ACF and RSC, two remodelers that respectively enable heterochromatin and euchromatin formation. Below we discuss the biological implications of our findings.

Nucleosome spacing and density regulate the properties of condensed chromatin

Chromatin condensation depends on inter-nucleosomal interactions. Therefore, nucleosome density is expected to influence the formation and compaction of condensates, and we systematically tested this prediction. Keeping DNA concentrations constant, we found that median densities of 4.6 nucleosomes per kilobase yielded condensates with nucleosome concentrations comparable to that in vivo, densities of 2.9 nucleosomes per kb yielded condensates with a fivefold lower concentration of nucleosomes, and densities of 1 nucleosome per kb did not yield detectable condensates. Furthermore, condensates formed by chromatin assembled on the native S3 sequence showed increased viscosity relative to condensates from chromatin with uniform, regularly spaced nucleosomes at comparable density. Recent cryo-electron tomography studies of native mammalian chromatin show a high proportion of irregularly spaced nucleosomes, and find that such chromatin is found in short intrafiber stacks of nucleosomes in cis interspersed with interfiber interactions in trans (*43*). By contrast, regularly spaced nucleosome arrays appear to contain a greater proportion of intrafiber nucleosome stacks (*43*–*45*). These differences may result in more stable interfiber interactions with irregularly spaced nucleosomes, explaining the greater viscosity.

Nucleosome-scale remodeling can explain meso-scale consequences

We found that ACF and RSC had different effects within condensed chromatin. We propose that these differences arise from two features: (i) how ACF and RSC bind and remodel nucleosomes (Fig. 5H) and (ii) their residency times on nucleosomes during ATP hydrolysis. Compared with ACF, RSC—which is bigger—is expected to occlude a larger region of the nucleosome and therefore have a larger effect on disrupting internucleosomal interactions (*35*, *37*, *46*). However, during ATP hydrolysis, the residency time of RSC on nucleosomes has been shown to be shorter than that of ACF (*42*). We propose that ATP hydrolysis switches RSC between nucleosome-bound states that inhibit internucleosomal interactions and nucleosome-free states that allow internucleosomal interactions (Fig. 5H). We speculate that such ATP-driven cycling between states transiently and locally disrupts internucleosomal interactions without globally dissolving the condensate. Such a cycle may increase the local dynamics within condensed chromatin. RSC catalyzed whole condensate motion despite being substantially substoichiometric relative to nucleosomes (Fig. 5H). This result suggests that disrupting internucleosomal interactions can have long-range cooperative effects.

Chromatin condensates also seemed to inherently limit remodeler concentrations. Both ACF and RSC, when added in stoichiometric concentrations to nucleosomes, only achieved substoichiometric

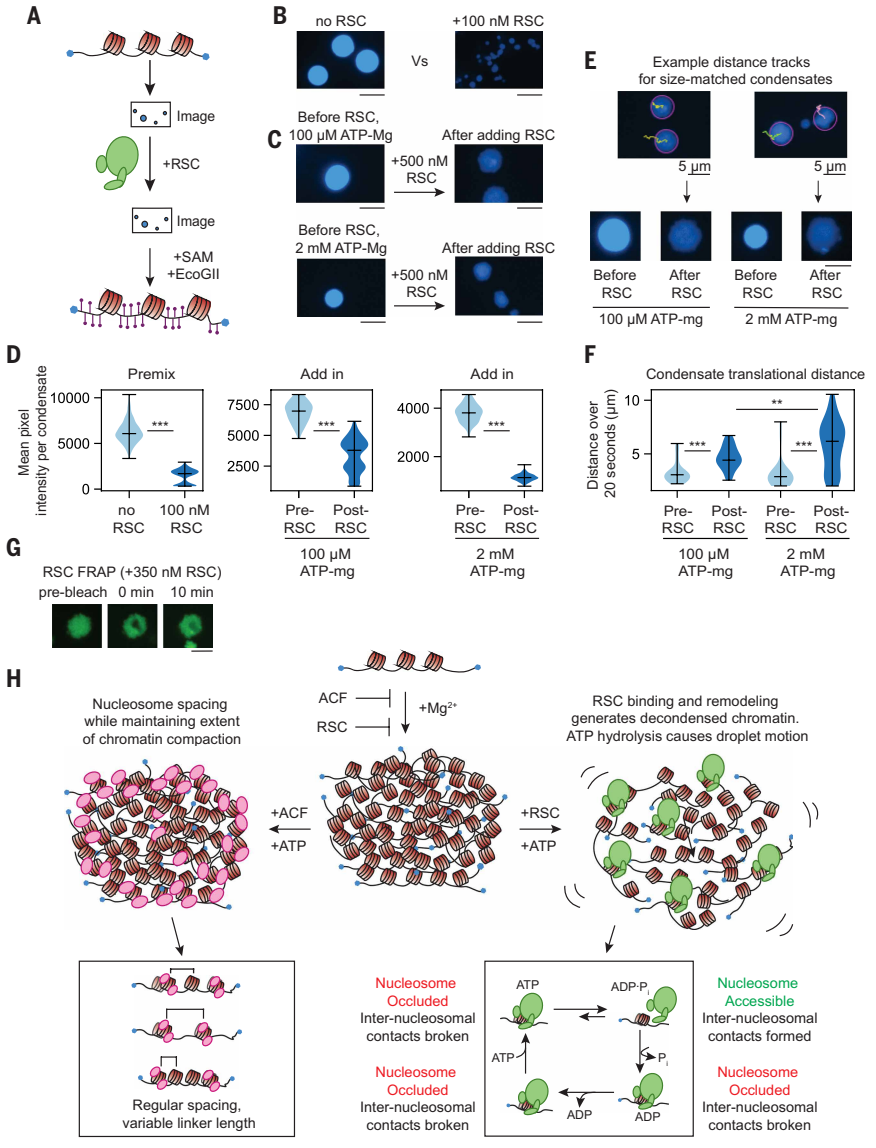

Fig. 5. RSC decondenses chromatin condensates and increases condensate motion in an ATP-dependent manner. (**A**) Scheme of RSC add-in experimental workflow. (**B**) Confocal images of chromatin condensates for the RSC premix experiment (scheme shown in Fig. 4A) in conditions with 220 nM nucleosome and 100 μM ATP-Mg. Estimated mean nucleosome concentration inside condensates is 38 μM (control reaction) and 9 μM (+100 nM RSC reaction). (**C**) RSC add-in experiment as shown in (A), performed under conditions with either 100 μM ATP-Mg or 2 mM ATP-Mg and 300 nM nucleosome. Estimated mean nucleosome concentration inside the condensates is 43 μM (before RSC, 100 μM ATP-mg), 21 μM (after RSC, 100 μM ATP-mg), 21 μM (before RSC, 2 mM ATP-mg), and 7 μM (after RSC, 2 mM ATP-mg). (**D**) Violin plots of mean condensate intensity for premix (left) and add-in experiments in (A) and (B) for condensates 2 to 6 μm in diameter (right). For premix (left to right): 610 and 2481 condensates were selected. For add-in (left to right): 165, 752, 189, and 814 condensates were selected. (**E**) Example traces of condensate *xy* translational distance over 20 seconds. Distance analysis was limited to condensates with diameter of approximately 5 μm. (**F**) Violin plot of size-matched condensate distance before and after RSC add-in. (Left to right) 70, 28, 24, and 148 condensates were selected. (**G**) Confocal images of RSC add-in using AF488-labeled RSC, 488 channel. Images are from 350 nM AF488-RSC add-in under conditions with 100 μM ATP-Mg. The molar ratio of nucleosome to RSC inside condensates is 13:1. (**H**) Model for chromatin condensation and remodeling within the condensate by ACF or RSC. All scale bars are 5 μm.

enrichment within condensates. The network of internucleosomal interactions within condensates may limit the remodeler molecules that can be accommodated. Thus, diffusion of a remodeler through a chromatin condensate would be regulated by both the off rate of the remodeler and the kinetics of breaking the local network of internucleosomal interactions.

In vivo, remodelers likely need to engage nucleosomes in at least two different contexts: in open chromatin states prior to condensation, and in states where the chromatin is condensed. ACF has been implicated in regulating heterochromatin (*8*, *47*). Although ACF concentration is estimated as 150 nM in certain mammalian nuclei (*48*), there is evidence that ACF concentrates in dense foci at newly replicating heterochromatin, raising the possibility that the ratio of ACF to nucleosomes increases substantially in this context. We speculate that newly replicating heterochromatin would be prevented from prematurely condensing by stoichiometric ACF binding and remodeling. By contrast, in the context of an existing heterochromatin domain, our findings imply that ACF can maintain the nucleosome spacing within heterochromatin without decondensing chromatin. ACF's slow diffusion through condensed chromatin may also allow for its long-term localization within heterochromatin. In contrast to ACF, we found that RSC decondensed preformed chromatin condensates in an ATP hydrolysis–dependent manner. It is well-established that chromatin decondensation correlates with transcription, but genomic studies cannot evaluate the effects of RSC on chromatin condensation in a transcription-independent manner, as RSC mutations affect transcription (*16*, *49*). Our approach reveals that RSC remodeling does induce transcription-independent chromatin decondensation, which likely contributes to decondensation of active gene promoters in vivo. Additionally, we speculate that the increased condensate motion caused by RSC may enable faster local diffusion of the transcription machinery and other proteins through the viscous environment of condensed chromatin.

Our findings demonstrate that ATP-dependent remodelers do not generically act as molecular stir bars; rather, their mesoscale effects on chromatin derive from their specific, nucleosome-scale interactions and activities. Future work is needed to clarify whether other nucleosome remodelers that catalyze distinct transformations of nucleosomes also have distinct effects on mesoscale chromatin dynamics. We anticipate that future cellular studies using high resolution microscopy to measure chromatin dynamics will help address the extent to which remodelers regulate chromatin condensation in vivo.

Materials and methods

Construction of *Cyp3a11* dsDNA-producing bacterial vector

A 3.2-kb stretch of Cyp3a11 was PCR-amplified from mouse genomic DNA. This fragment was cloned into the puc18 plasmid using Gibson Cloning (NEBuilder HiFi DNA Assembly Master Mix, NEB) and transformed into DCM-/DAM-competent cells. Colonies were isolated and miniprepped (Qiagen) and plasmid sequence was validated via Primordium Sequencing.

Expression and purification of recombinant proteins

Recombinant histones from *Xenopus laevis* were expressed and purified in *Escherichia coli* as previously described (*50*). The Snf2h ATPase

was purified from *E. coli* (*30*) and the human ACF complex was purified from Sf9 insect cells as previously described (*30*) with a minor modification. ACF1-FLAG and SNF2H were expressed on the same plasmid via infection with baculovirus.

The RSC2 C-terminally 3xFLAG-tagged yeast strain was generated by E. Muñoz and L. Hsieh. The FLAG-tagged RSC complex was purified from yeast as previously described (*51*) with a minor modification. The RSC complex was purified over a Mono Q 5/50 column in order to remove excess FLAG peptide. After elution from the column, RSC was dialyzed into storage buffer (25 mM HEPES pH 7.5, 1 mM EDTA, 10% glycerol, 0.02% NP-40, 100 mM KCl, 1 mM DTT).

Protein concentrations were determined via SYPRO red (Thermo Fisher) staining of a sodium dodecyl sulfate (SDS)–polyacrylamide gel electrophoresis gel with bovine serum albumin standards.

Array DNA purification

12x601+47 plasmid was a generous gift from the Rosen lab. The 12x601 plasmid was transformed into Stabl3 cells and purified via Giga Prep (Qiagen). The 12x601 insert was isolated from the plasmid backbone via restriction digest (EcoRV-HF) and size exclusion chromatography. After size exclusion, purified 12x601 insert was precipitated in ethanol and resuspended in 1X TE.

The *Cyp3a11* sequence was digested from the puc18 backbone via PciI and BamHI and similarly purified.

DNA labeling

Cypa11 (S3) DNA was end-labeled with Alexa Fluor-647-aha-dCTP or Alexa Fluor-555-aha-dCTP (Thermo) using the Klenow fragment.

12x601 array DNA was first digested with XhoI to generate a 5′ overhang, then similarly labeled with Alexa Fluor-647-aha-dCTP using the Klenow fragment. S1 was digested with NheI and similarly labeled. Labeling efficiency was quantified via NanoDrop UV-Vis.

Histone octamer purification

Histones were refolded in high salt buffer together to form octamer. Octamer was purified by size-exclusion chromatography as previously described (*50*). Acidic patch mutant histone H2A (Histone H2A E61A, E64A, D90A, D92A) expression plasmid was a generous gift from the Tan lab at Penn State. H4Δ1-20 plasmid was generated by previous lab members.

Chromatin assembly

Chromatin was assembled using salt gradient dialysis with varying ratios of histone octamer:DNA (*50*). DNA concentration was determined after assembly via Nanodrop.

Sucrose gradient

After salt gradient dialysis, 12x601 chromatin arrays were added to a 10 to 30% sucrose gradient (10 mM Tris pH 7.5, 1 mM EDTA, 1 mM DTT, sucrose) and spun for 16 hours at 22,900 RPM. Fractions containing assembled nucleosomes were concentrated using 10,000 MWCO centrifugal concentrators (Amicon).

Protein labeling

Remodelers were labeled with Alexa Fluor-488 C_5 Maleimide (Thermo). Purified remodeler was dialyzed overnight to remove DTT, then reduced via 10-fold molar excess of TCEP relative to the protein. Dye was resuspended in DMSO. Labeling was done with 20-fold molar excess dye relative to the protein for 30 min at room temperature, then quenched with excess DTT. Free dye was removed from labeled protein via overnight dialysis in 500mL buffer using a pump to continuously flow buffer (1L total buffer was flowed through). Buffer compositions were identical to original buffer compositions before labeling. Protein concentration was calculated via Nanodrop and SYPRO red (Thermo Fisher) staining of SDS–polyacrylamide gel electrophoresis gel with bovine serum albumin standards. Labeling efficiency was calculated via Nanodrop UV Vis.

Mono-nucleosome remodeling assay

Mono-nucleosomes were prepared via salt gradient dialysis from purified *X. laevis* histone octamers and PCR-purified Widom601 sequence + 80 bp or Cy5-40bp-Widom601 sequence-40 bp as previously described. Mono-nucleosomes were remodeled via ACF, Snf2h, and RSC under single turnover saturating enzyme and saturating ATP conditions. Reactions contained 30 mM HEPES pH 7.5, 50 mM KCl, 1 mM $MgCl_2$, 0.02% NP-40, 5 mM ATP-$MgCl_2$. Time points taken from the reaction were quenched with 0.4 mg/ml puc19, 20 mM ADP, 8% glycerol. Nucleosomes were loaded on a 6% polyacrylamide gel in 0.5x TBE and run at 150V for 2 hours. DNA bands were imaged using the Cy5 channel or SybrSafe stain on a Typhoon imager (GE Life Sciences).

Preparation of microscopy plates

Corning 384-well microscopy plates were mPEGylated and passivated with bovine serum albumin (BSA) as previously described (*23*).

Phase separation remodeling reactions

Unless otherwise stated, phase separation reactions contained 20 nM chromatin array, 100 mM KCl, 4-7% glycerol, 25 mM HEPES pH 7.5, 5 mM DTT, 2 mM free Mg2+, 0.5 mM EDTA. ATP-Mg concentration was either 100 μM or 2 mM.

Phase separation reactions in Fig. 1 contained 75 mM KCl, 2.5% glycerol, 20 mM HEPES pH 7.5, 2 mM ATP, 4 mM Mg2+, 0.5 mM EDTA, 20 nM array.

Phase separation reaction conditions for the 12x601 array were 150 mM NaCl, 5% glycerol, 25 mM Tris-Cl pH 7.5, 1 mM $MgCl_2$, 5 mM DTT.

Reactions were mixed and added to a PEGylated and BSA-passivated microscopy plate. Reactions were sealed with PCR foil to prevent evaporation. After 1 to 1.5 hours, foil was removed and reactions were imaged using a spinning disk confocal microscope. For add-in reactions, protein was added after initial imaging and gently pipetted several times to mix. 30 min after mixing, add-in reactions were imaged again and FRAPped.

After imaging, excess ADP (34 mM final) was added to reactions and mixed with a pipette several times to quench ATP-dependent remodeling. All phase separation conditions in Figs. 1 to 5 were repeated with at least one biological replicate except for Figs. 3E and 5G, where we instead tested a series of ACF and RSC concentrations, respectively (fig. S11E and fig. S13, H and I).

For the ATP titration in fig. S13F, chromatin reactions were incubated in the foil-sealed phasing plate overnight before imaging.

For the RSC add in experiments in figs. S12, S16, and S17, chromatin was first incubated overnight in the foil-sealed phasing plate before imaging and RSC add in. RSC was added after initial imaging and gently pipetted several times to mix. 30 min after mixing, add-in reactions were imaged again and FRAPped.

After imaging, excess ADP (34 mM final) was added to reactions and mixed with a pipette several times to quench ATP-dependent remodeling. SAMOSA-ChAAT reactions were then prepared in 100 μl with final reaction conditions 20 mM HEPES pH 7.5, 1 mM SAM, 2 μl high concentration EcoGII, 2.5×10^4 U ml^{-1}. Downstream processing was identical to other SAMOSA-ChAAT reactions.

Remodeler depletion experiments

ACF: Reaction conditions were 100 mM KCl, 7% glycerol, 25 mM HEPES pH 7.5, 1.5 mM MgCl2, 5 mM DTT, 100 μM ATP-Mg, 20 nM chromatin array, and 260 nM ACF.

RSC: Reaction conditions were 100 mM KCl, 4% glycerol, 25 mM HEPES pH 7.5, 1.5 mM MgCl2, 5 mM DTT, 100 μM ATP-Mg, 20 nM chromatin array, and 100 nM or 350 nM RSC.

Remodeler was dialyzed first for 2 hours, then overnight at 4°C to remove DTT and FLAG peptide (in the case of ACF). Remodeling reactions were 13 µl with the conditions described above. Reactions were mixed and left at RT for two hours.

Magnetic anti-FLAG M2 beads (Thermo) were equilibrated by washing twice in 300 mM KCl, 4 or 7% glycerol, 25 mM HEPES pH 7.5, 1.5 mM MgCl2. 2 µl of bead slurry was used per 13 µl remodeling reaction. After remodeling, 1 µl of 3 M KCl was added to each remodeling reaction and reactions were then added to anti-FLAG beads. Beads were gently resuspended via flicking and incubated for 20 min at RT. After 20 min, beads were pelleted on a magnet and supernatant was removed. For reactions with 1x bead incubation, salt was then diluted to 150 mM KCl by 2x dilution into reaction buffer with no salt so that total reaction volume was 26 µl. For reactions with 2x bead incubation, the supernatant from the beads was added to another 2 µl of equilibrated anti-FLAG beads and incubated for an additional 20 min before 2x dilution into reaction buffer with no salt. Reactions were added to BSA-passivated microscopy wells and left to sit for 1 hour before confocal imaging at 100x. After imaging, reactions were removed from phasing plate, quenched with 7 µl of 95 mM ADP, and left for 5 min. SAMOSA-ChAAT reactions were then prepared in 100 µl with final reaction conditions 20 mM HEPES pH 7.5, 1 mM SAM, 2 µl high concentration EcoGII, 2.5×10^4 U ml^{-1}. Downstream processing was identical to other SAMOSA-ChAAT reactions.

Microscopy

Data for this study were acquired at the Center for Advanced Light Microscopy at UCSF. Confocal microscopy images were acquired using a Nikon Ti Eclipse microscope base equipped with either a Yokogawa CSU-22 spinning disk confocal unit or CREST X-Light V2 L-FOV Spinning Disk confocal unit, 100 X 1.40 NA oil objective, and an Andor Zyla 4.2 camera. Fluorescence Recovery After Photobleaching (FRAP) was done with a 473 nm laser (Vortran) and Rapp UGA-40 photobleaching system. Widefield microscopy images in fig. S6 were acquired using a Nikon Ti Eclipse microscope base equipped with a 20 × 0.75 NA objective and a Nikon DS-Qi2 camera.

Image intensity and displacement quantification

Image analysis was done with ImageJ (Version 2.14) (*52*). Unless otherwise described, image brightness and contrast were normalized for a given panel of images and images were collected under identical microscopy settings. Mean pixel intensities per chromatin condensate were calculated in ImageJ from .tif files. Condensates were picked using the Otsu algorithm and auto thresholding using minimum cutoffs of 0.2 circularity and 0.5 μm^2. Condensates on image edges were excluded from analysis. Script is available in the Zenodo repository.

For intensity histograms, the number of bins was set to 10% of the total number of condensates unless the number of bins exceeded 40, in which case the number of bins was capped at 40, or if the number of bins was below 7, in which case the bin number was set to 7. Statistical significance of the difference between sample metrics (mean condensate intensity, distance, size) was determined by performing two-tailed independent *t* tests in Scipy (Scipy.ttest.ind()).

Condensate 2D circularity was defined as circularity = 4pi(area/perimeter^2) and computed in ImageJ. Translational displacement tracking analysis of chromatin droplets in the xy plane was done with the Trackmate plugin in ImageJ (*53*). Exact parameters used were: diameter = 3.0 µm for experiment in Fig. 5 or 5.0 µm for experiment in fig. S16, subpixel localization, max distance = 3 µm, gap-closing distance = 5 µm, gap-closing max frame gap = 5 µm, auto thresholding. To directly compare the high mobility condensate populations across conditions in Fig. 5, a minimum threshold of 2 µm was applied. Full distributions without thresholding are showing in fig. S13G.

Correlating chromatin condensate area change with condensate intensity change after adding RSC

The fold change in condensate area was computed by dividing the mean condensate area after adding RSC by the mean condensate area before adding RSC (area distributions shown in fig. S15). For the low ATP conditions (100 µM ATP-mg), the fold change in area was 44.64/24.08 = 1.85. For the high ATP condition (2 mM ATP-mg), the fold change in area was 8.35/3.67 = 2.28.

Fold change in volume = (fold change in area)$^{3/2}$

Fold change in volume after adding RSC in conditions with 100 µM ATP-mg: 2.5

Fold change in volume after adding RSC in conditions with 2 mM ATP-mg: 3.4

This ratio should be proportional to the decrease in mean pixel intensity per condensate after adding RSC if chromatin is maintained within the condensates after adding RSC.

The decrease in pixel intensity per condensate for the AF647 channel was computed by dividing the mean pixel intensity per condensate before adding RSC by the mean pixel intensity per condensate after adding RSC (pixel intensity distributions shown in Fig. 5D).

Fold change in pixel intensity per condensate after adding RSC in in conditions with 100 µM ATP-mg: 2.08

Fold change in pixel intensity per condensate after adding RSC in in conditions with 2 mM ATP-mg: 3.15

Calculating nucleosome concentration

Nucleosome concentration in phase separation reactions was determined by multiplying the concentration of chromatin array in the reaction by the median number of nucleosomes per molecule.

Nucleosome concentration inside condensates was determined using the mean AF647 channel pixel intensity per condensate and a standard curve of free AF647 dye using the same exposure and laser power as samples (fig. S1). The mean pixel intensity per condensate was divided by two because each chromatin molecule has two fluorescent labels (Fig. 1A), and this value was divided by the slope determined by the standard curve (1235.5/µM), then multiplied by the median number of nucleosomes per molecule determined for that chromatin assembly.

$$\frac{(mean\ pixel\ intensity\ per\ condensate)}{2} = \frac{1235.5}{\mu M} \times condensate\,[DNA]$$

$$Condensate\,[nucleosome] = \frac{(mean\ pixel\ intensity\ per\ condensate)}{2 \times 1235.5} \times median\ nucleosomes\ per\ molecule\ DNA$$

Calculating remodeler concentration inside condensates

Remodeler concentrations were determined using the mean AF488 channel pixel intensity per condensate and a standard curve of free AF488 dye using the same exposure and laser power as samples (fig. S1). The mean pixel intensity per condensate was divided by the molar ratio of label/protein determined via Nanodrop and gel, and this value was divided by the slope determined using the AF488 standard curve.

SAMOSA-ChAAT on chromatin arrays

SAMOSA-ChAAT was performed on chromatin arrays using the non-specific adenine methyltransferase EcoGII (NEB, high concentration stock 2.5×10^4 U ml^{-1}) as previously described (*25*, *28*) with minor modifications. The phase separation reaction volume was removed from the microscopy plate and diluted to 100 µl in 1xCutSmart buffer + 1 mM SAM + 1 µl EcoGII. Reactions were mixed and incubated at 37C for 30 min. After 30 min, 10 µl of 10% SDS and 2.5 µl Proteinase K (20 mg/ml) was added to each reaction and mixed with a pipette. Reactions were incubated at 65C for 2 hours or overnight. Methylated

DNA was purified from these reactions via 1X SPRI Select Beads. All SAMOSA-ChAAT conditions in Figs. 1 to 5 were repeated with at least one biological replicate except for Fig. 3C.

Pacbio library preparation and sequencing

Fluorophores were removed from DNA by restriction digest in 50 µl of 1x CutSmart with 1 µl SmaI and 1 µl BsiEI. Restriction digests were incubated for 15 min at room temperature, then 15 min at 60C. DNA was purified from these reactions via 1X SPRI Select Beads. Entire remodeling reactions were used as input for PacBio SMRTbell library preparation. SMRTbell preparation of libraries was done using the SMRTbell template express kit 3.0 and included DNA damage repair, end repair, SMRTbell ligation, and exonuclease cleanup according to the manufacturer's instruction. After exonuclease cleanup and purification via 1x v/v SMRTbell cleanup beads, DNA concentration was measured by Qubit High Sensitivity DNA Assay (1 µeach sample). Data was collected over 30-hour Sequel II movie runs with 2 hours pre-extension time and 2.1 polymerase.

SMRT data processing

Sequencing reads were processed as homogenous samples as described in (*25*) with slight variations.

Model training

For training neural network, SMM, and SVD models on fully methylated and unmethylated controls, raw subreads were processed identically to homogenous samples (*25*) and models were trained as previously described. The Hidden Markov model was structured similarly to (*25*) but was refactored from pomegranate to use cython and numba.

Chromatin sample processing

Raw sequencing reads from chromatin samples were processed using software from Pacific Biosciences:

1. Generate circular consensus sequences (CCS)

CCS were generated for each sequencing cell using ccs 6.9.99. The–hifi-kinetics flag was used to generate kinetics information (interpulse duration, or IPD) for each base of each consensus read. Values were stored for each base as 50*(mean logIPD) + 1.

2. Demultiplex consensus reads

Consensus reads were demultiplexed using lima. The flag '–same' was passed as libraries were generated with the same barcode on both ends. This produces a BAM file for the consensus reads of each sample.

3. Align consensus reads to the reference genome

pbmm2, the pacbio wrapper for minimap2 (*54*), was run on each CCS BAM file (the output of step 2) to align reads to the reference sequence, producing a BAM file of aligned consensus reads.

Extracting interpulse duration measurements

The IPD values were accessed from the aligned, demultiplexed consensus BAM files. Values were transformed so that each value represented the $\log_{10}$IPD, in order to match the $\log_{10}$IPD values that were used to train the models.

Processed data analysis

All processed data analyses and associated scripts are available at Zenodo (*55*). All analyses were computed using python. Plots were constructed via Matplotlib. Each analysis is briefly described below:

Defining inaccessible regions and counting nucleosomes

Heatmaps of inaccessible and accessible bases were generated from binarized accessibility arrays identically to (*25*).

Inaccessible regions were called from HMM output data identically to (*25*). Briefly, inaccessible regions were defined as continuous stretches with accessibility ≤0.5. Periodic peaks were observed that approximated sizes of regions containing one, two, three, or more nucleosomes. Cutoffs for each size were manually defined using the histogram of inaccessible region lengths (fig. S3). Importantly, this histogram contained all data from the low, medium, and high nucleosome density chromatin samples shown in Fig. 1. For the histograms in Fig. 1, all molecules are plotted.

Autocorrelations were calculated using Python, then clustered. Leiden clustering analyses were performed identically to (*25*).

SAMOSA-ChAAT quality control validation

Correlation of average methylation per base for fluorescently end-labeled *Cyp3a11* vs unlabeled *Cyp3a11* is shown in fig. S18A. Correlation of average methylation per base for chromatin methylated in a test tube vs methylated in a microscopy plate well shown in fig. S18B. Correlation between SAMOSA-ChAAT technical replicates is shown in fig. S18C.

REFERENCES AND NOTES

1. E. Lieberman-Aiden *et al.*, Comprehensive mapping of long-range interactions reveals folding principles of the human genome. *Science* **326**, 289–293 (2009). doi: 10.1126/science.1181369; pmid: 19815776
2. J. Dekker, Mapping in vivo chromatin interactions in yeast suggests an extended chromatin fiber with regional variation in compaction. *J. Biol. Chem.* **283**, 34532–34540 (2008). doi: 10.1074/jbc.M806479200; pmid: 18930918
3. C. R. Clapier, J. Iwasa, B. R. Cairns, C. L. Peterson, Mechanisms of action and regulation of ATP-dependent chromatin-remodelling complexes. *Nat. Rev. Mol. Cell Biol.* **18**, 407–422 (2017). doi: 10.1038/nrm.2017.26; pmid: 28512350
4. C. Y. Zhou, S. L. Johnson, N. I. Gamarra, G. J. Narlikar, Mechanisms of ATP-Dependent Chromatin Remodeling Motors. *Annu. Rev. Biophys.* **45**, 153–181 (2016). doi: 10.1146/annurev-biophys-051013-022819; pmid: 27391925
5. N. Krietenstein *et al.*, Genomic Nucleosome Organization Reconstituted with Pure Proteins. *Cell* **167**, 709–721.e12 (2016). doi: 10.1016/j.cell.2016.09.045; pmid: 27768892
6. K. Luger, A. W. Mäder, R. K. Richmond, D. F. Sargent, T. J. Richmond, Crystal structure of the nucleosome core particle at 2.8 A resolution. *Nature* **389**, 251–260 (1997). doi: 10.1038/38444; pmid: 9305837
7. T. Ito, M. Bulger, M. J. Pazin, R. Kobayashi, J. T. Kadonaga, ACF, an ISWI-containing and ATP-utilizing chromatin assembly and remodeling factor. *Cell* **90**, 145–155 (1997). doi: 10.1016/S0092-8674(00)80321-9; pmid: 9230310
8. D. V. Fyodorov, M. D. Blower, G. H. Karpen, J. T. Kadonaga, Acf1 confers unique activities to ACF/CHRAC and promotes the formation rather than disruption of chromatin in vivo. *Genes Dev.* **18**, 170–183 (2004). doi: 10.1101/gad.1139604; pmid: 14752009
9. T. Tsukiyama, J. Palmer, C. C. Landel, J. Shiloach, C. Wu, Characterization of the imitation switch subfamily of ATP-dependent chromatin-remodeling factors in Saccharomyces cerevisiae. *Genes Dev.* **13**, 686–697 (1999). doi: 10.1101/gad.13.6.686; pmid: 10090725
10. P. D. Varga-Weisz *et al.*, Chromatin-remodelling factor CHRAC contains the ATPases ISWI and topoisomerase II. *Nature* **388**, 598–602 (1997). doi: 10.1038/41587; pmid: 9252192
11. G. Längst, E. J. Bonte, D. F. V. Corona, P. B. Becker, Nucleosome movement by CHRAC and ISWI without disruption or trans-displacement of the histone octamer. *Cell* **97**, 843–852 (1999). doi: 10.1016/S0092-8674(00)80797-7; pmid: 10399913
12. Y. Lorch, M. Zhang, R. D. Kornberg, RSC unravels the nucleosome. *Mol. Cell* **7**, 89–95 (2001). doi: 10.1016/S1097-2765(01)00157-5; pmid: 11172714
13. S. Ramachandran, G. E. Zentner, S. Henikoff, Asymmetric nucleosomes flank promoters in the budding yeast genome. *Genome Res.* **25**, 381–390 (2015). doi: 10.1101/gr.182618.114; pmid: 25491770
14. B. R. Cairns *et al.*, RSC, an essential, abundant chromatin-remodeling complex. *Cell* **87**, 1249–1260 (1996). doi: 10.1016/S0092-8674(00)81820-6; pmid: 8980231
15. M. Floer *et al.*, A RSC/nucleosome complex determines chromatin architecture and facilitates activator binding. *Cell* **141**, 407–418 (2010). doi: 10.1016/j.cell.2010.03.048; pmid: 20434983
16. T. H. Hsieh *et al.*, Mapping Nucleosome Resolution Chromosome Folding in Yeast by Micro-C. *Cell* **162**, 108–119 (2015). doi: 10.1016/j.cell.2015.05.048; pmid: 26119342
17. K. Yen, V. Vinayachandran, K. Batta, R. T. Koerber, B. F. Pugh, Genome-wide nucleosome specificity and directionality of chromatin remodelers. *Cell* **149**, 1461–1473 (2012). doi: 10.1016/j.cell.2012.04.036; pmid: 22726434
18. A. Klein-Brill, D. Joseph-Strauss, A. Appleboim, N. Friedman, Dynamics of Chromatin and Transcription during Transient Depletion of the RSC Chromatin Remodeling Complex. *Cell Rep.* **26**, 279–292.e5 (2019). doi: 10.1016/j.celrep.2018.12.020; pmid: 30605682
19. S. Kubik *et al.*, Sequence-Directed Action of RSC Remodeler and General Regulatory Factors Modulates +1 Nucleosome Position to Facilitate Transcription. *Mol. Cell* **71**, 89–102.e5 (2018). doi: 10.1016/j.molcel.2018.05.030; pmid: 29979971

20. E. Oberbeckmann, K. Quililan, P. Cramer, A. M. Oudelaar, In vitro reconstitution of chromatin domains shows a role for nucleosome positioning in 3D genome organization. *Nat. Genet.* **56**, 483–492 (2024). doi: 10.1038/s41588-023-01649-8; pmid: 38291333
21. A. G. Larson, G. J. Narlikar, The Role of Phase Separation in Heterochromatin Formation, Function, and Regulation. *Biochemistry* **57**, 2540–2548 (2018). doi: 10.1021/acs.biochem.8b00401; pmid: 29644850
22. S. Hihara *et al.*, Local nucleosome dynamics facilitate chromatin accessibility in living mammalian cells. *Cell Rep.* **2**, 1645–1656 (2012). doi: 10.1016/j.celrep.2012.11.008; pmid: 23246002
23. B. A. Gibson *et al.*, Organization of chromatin by intrinsic and regulated phase separation. *Cell* **179**, 470–484.e421 (2019). doi: 10.1016/j.celrep.2012.11.008; pmid: 23246002
24. J. C. Hansen, K. Maeshima, M. J. Hendzel, The solid and liquid states of chromatin. *Epigenetics Chromatin* **14**, 50 (2021). doi: 10.1186/s13072-021-00424-5; pmid: 34717733
25. N. J. Abdulhay *et al.*, Nucleosome density shapes kilobase-scale regulation by a mammalian chromatin remodeler. *Nat. Struct. Mol. Biol.* **30**, 1571–1581 (2023). doi: 10.1038/s41594-023-01093-6; pmid: 37696956
26. B. A. Gibson *et al.*, In diverse conditions, intrinsic chromatin condensates have liquid-like material properties. *Proc. Natl. Acad. Sci. U.S.A.* **120**, e2218085120 (2023). doi: 10.1073/pnas.2218085120; pmid: 37094140
27. K. Maeshima *et al.*, A Transient Rise in Free Mg^{2+} Ions Released from ATP-Mg Hydrolysis Contributes to Mitotic Chromosome Condensation. *Curr. Biol.* **28**, 444–451.e6 (2018). doi: 10.1016/j.cub.2017.12.035; pmid: 29358072
28. N. J. Abdulhay *et al.*, Massively multiplex single-molecule oligonucleosome footprinting. *eLife* **9**, e59404 (2020). doi: 10.7554/eLife.59404; pmid: 33263279
29. J. G. Yang, T. S. Madrid, E. Sevastopoulos, G. J. Narlikar, The chromatin-remodeling enzyme ACF is an ATP-dependent DNA length sensor that regulates nucleosome spacing. *Nat. Struct. Mol. Biol.* **13**, 1078–1083 (2006). doi: 10.1038/nsmb1170; pmid: 17099699
30. N. Gamarra, S. L. Johnson, M. J. Trnka, A. L. Burlingame, G. J. Narlikar, The nucleosomal acidic patch relieves auto-inhibition by the ISWI remodeler SNF2h. *eLife* **7**, e35322 (2018). doi: 10.7554/eLife.35322; pmid: 29664398
31. X. He, H. Y. Fan, G. J. Narlikar, R. E. Kingston, Human ACF1 alters the remodeling strategy of SNF2h. *J. Biol. Chem.* **281**, 28636–28647 (2006). doi: 10.1074/jbc.M603008200; pmid: 16877760
32. T. R. Blosser, J. G. Yang, M. D. Stone, G. J. Narlikar, X. Zhuang, Dynamics of nucleosome remodelling by individual ACF complexes. *Nature* **462**, 1022–1027 (2009). doi: 10.1038/nature08627; pmid: 20033040
33. S. L. Johnson, G. J. Narlikar, ATP Hydrolysis Coordinates the Activities of Two Motors in a Dimeric Chromatin Remodeling Enzyme. *J. Mol. Biol.* **434**, 167653 (2022). doi: 10.1016/j.jmb.2022.167653; pmid: 35659534
34. P. Vizjak *et al.*, ISWI catalyzes nucleosome sliding in condensed nucleosome arrays. *Nat. Struct. Mol. Biol.* **31**, 1331–1340 (2024). doi: 10.1038/s41594-024-01290-x; pmid: 38664566
35. F. R. Wagner *et al.*, Structure of SWI/SNF chromatin remodeller RSC bound to a nucleosome. *Nature* **579**, 448–451 (2020). doi: 10.1038/s41586-020-2088-0; pmid: 32188943
36. Y. Ye *et al.*, Structure of the RSC complex bound to the nucleosome. *Science* **366**, 838–843 (2019). doi: 10.1126/science.aay0033; pmid: 31672915
37. A. B. Patel *et al.*, Architecture of the chromatin remodeler RSC and insights into its nucleosome engagement. *eLife* **8**, e54449 (2019). doi: 10.7554/eLife.54449; pmid: 31886770
38. R. W. Baker *et al.*, Structural insights into assembly and function of the RSC chromatin remodeling complex. *Nat. Struct. Mol. Biol.* **28**, 71–80 (2021). doi: 10.1038/s41594-020-00528-8; pmid: 33288924
39. C. E. Rowe, G. J. Narlikar, The ATP-dependent remodeler RSC transfers histone dimers and octamers through the rapid formation of an unstable encounter intermediate. *Biochemistry* **49**, 9882–9890 (2010). doi: 10.1021/bi101491u; pmid: 20853842
40. B. T. Harada *et al.*, Stepwise nucleosome translocation by RSC remodeling complexes. *eLife* **5**, e10051 (2016). doi: 10.7554/eLife.10051; pmid: 26895087
41. P. D. Partensky, G. J. Narlikar, Chromatin remodelers act globally, sequence positions nucleosomes locally. *J. Mol. Biol.* **391**, 12–25 (2009). doi: 10.1016/j.jmb.2009.04.085; pmid: 19450608
42. J. M. Kim *et al.*, Dynamic 1D search and processive nucleosome translocations by RSC and ISW2 chromatin remodelers. *eLife* **12**, RP91433 (2024). doi: 10.7554/eLife.91433; pmid: 38497611
43. N. Jentink, C. Purnell, B. Kable, M. T. Swulius, S. A. Grigoryev, Cryoelectron tomography reveals the multiplex anatomy of condensed native chromatin and its unfolding by histone citrullination. *Mol. Cell* **83**, 3236–3252.e7 (2023). doi: 10.1016/j.molcel.2023.08.017; pmid: 37683647
44. B. Dorigo *et al.*, Nucleosome arrays reveal the two-start organization of the chromatin fiber. *Science* **306**, 1571–1573 (2004). doi: 10.1126/science.1103124; pmid: 15567867
45. A. Routh, S. Sandin, D. Rhodes, Nucleosome repeat length and linker histone stoichiometry determine chromatin fiber structure. *Proc. Natl. Acad. Sci. U.S.A.* **105**, 8872–8877 (2008). doi: 10.1073/pnas.0802336105; pmid: 18583476
46. L. Li *et al.*, Structure of the ISW1a complex bound to the dinucleosome. *Nat. Struct. Mol. Biol.* **31**, 266–274 (2024). doi: 10.1038/s41594-023-01174-6; pmid: 38177688
47. N. Collins *et al.*, An ACF1-ISWI chromatin-remodeling complex is required for DNA replication through heterochromatin. *Nat. Genet.* **32**, 627–632 (2002). doi: 10.1038/ng1046; pmid: 12434153
48. F. Erdel, T. Schubert, C. Marth, G. Längst, K. Rippe, Human ISWI chromatin-remodeling complexes sample nucleosomes via transient binding reactions and become immobilized at active sites. *Proc. Natl. Acad. Sci. U.S.A.* **107**, 19873–19878 (2010). doi: 10.1073/pnas.1003438107; pmid: 20974961
49. L. Lopez-Serra, G. Kelly, H. Patel, A. Stewart, F. Uhlmann, The Scc2-Scc4 complex acts in sister chromatid cohesion and transcriptional regulation by maintaining nucleosome-free regions. *Nat. Genet.* **46**, 1147–1151 (2014). doi: 10.1038/ng.3080; pmid: 25173104
50. K. Luger, T. J. Rechsteiner, T. J. Richmond, Expression and purification of recombinant histones and nucleosome reconstitution. *Methods Mol. Biol.* **119**, 1–16 (1999). doi: 10.1385/1-59259-681-9:1; pmid: 10804500
51. C. Y. Zhou *et al.*, The Yeast INO80 Complex Operates as a Tunable DNA Length-Sensitive Switch to Regulate Nucleosome Sliding. *Mol. Cell* **69**, 677–688.e9 (2018). doi: 10.1016/j.molcel.2018.01.028; pmid: 29452642
52. C. A. Schneider, W. S. Rasband, K. W. Eliceiri, NIH Image to ImageJ: 25 years of image analysis. *Nat. Methods* **9**, 671–675 (2012). doi: 10.1038/nmeth.2089; pmid: 22930834
53. D. Ershov *et al.*, TrackMate 7: Integrating state-of-the-art segmentation algorithms into tracking pipelines. *Nat. Methods* **19**, 829–832 (2022). doi: 10.1038/s41592-022-01507-1; pmid: 35654950
54. H. Li, Minimap2: Pairwise alignment for nucleotide sequences. *Bioinformatics* **34**, 3094–3100 (2018). doi: 10.1093/bioinformatics/bty191; pmid: 29750242
55. C. M. Moore *et al.*, ATP-dependent remodeling of chromatin condensates reveals distinct mesoscale outcomes, Version v1, Zenodo (2025); https://zenodo.org/records/15595590.

ACKNOWLEDGMENTS

We thank J. Tretyakova for histone purification, L. Hsieh for RSC construction and invaluable advice, K. Harrington and S. Y. Kim for their expansive knowledge of the confocal microscope, M. Rosen (UT Southwestern) for the 12×601 plasmid, S. Nanda for mentorship, and all members of the Narlikar and Ramani labs for advice and discussion. We also thank B. Huang for noticing the movement of droplets with RSC and encouraging us to pursue it. **Funding:** This research was funded by NIH grant U01DK127421 to G.J.N. and V.R., grant R35GM127020 to G.J.N., and grant DP2-HG012442 to V.R. **Author contributions:** C.M. and U.K. purified the RSC. C.M. and Z.Z. purified the ACF. U.K. and U.S.C. assembled and purified the mono-nucleosomes. E.W. purified the 12×Widom601 DNA; M.O., K.W., S.W., I.I., and C.M. prepared samples for PacBio sequencing. C.M. performed and quantified all biochemical experiments. V.R. and G.J.N. conceived and oversaw the project. C.M., V.R., and G.J.N. participated in interpretation and discussion of the results and writing of the manuscript. **Competing interests:** G.J.N. is a co-founder of TippingPoint Biosciences. All other authors declare no competing interests. **Data and materials availability:** Raw and processed data will be made available at GEO: GSE299834. All scripts and notebooks used for data analysis are available at Zenodo (55). Plasmids will be made available upon request.

SUPPLEMENTARY MATERIALS

science.org/doi/10.1126/science.adr0018
Figs. S1 to S18; MDAR Reproducibility Checklist; Movies S1 to S12

Submitted 22 June 2024; resubmitted 3 March 2025; accepted 27 June 2025
10.1126/science.adr0018

ATP-dependent remodeling of chromatin condensates reveals distinct mesoscale outcomes

Camille Moore, Emily Wong, Upneet Kaur, Un Seng Chio, Ziling Zhou, Megan Ostrowski, Ke Wu, Iryna Irkliyenko, Sean Wang, Vijay Ramani, and Geeta J. Narlikar

Science **390** (6768), eadr0018. DOI: 10.1126/science.adr0018

Editor's summary

Eukaryotic DNA is packaged as chromatin, the basic unit of which is the nucleosome, around which about 150 base pairs of DNA are wrapped, limiting its accessibility. Chromatin remodelers mobilize nucleosomes to regulate replication and transcription. Moore *et al*. studied two major remodelers, ACF and RSC, in crowded chromatin by recreating phase-separated chromatin droplets in vitro. They found that both remodelers could enter and mobilize nucleosomes within droplets, but only RSC decompacted chromatin and increased droplet mobility. This decompaction likely enhances DNA accessibility in cells. Their findings suggest that remodelers differ in biological importance depending on their capacity to mobilize and decompact compacted chromatin. —Di Jiang

Science
AAAS

Supplementary Materials for

ATP-dependent remodeling of chromatin condensates reveals distinct mesoscale outcomes

Camille Moore *et al*.

Corresponding authors: Vijay Ramani, vijay.ramani@gladstone.ucsf.edu; Geeta J. Narlikar, geeta.narlikar@ucsf.edu

Science **390**, eadr0018 (2025)
DOI: 10.1126/science.adr0018

The PDF file includes:

Figs. S1 to S18

Other Supplementary Material for this manuscript includes the following:

MDAR Reproducibility Checklist
Movies S1 to S12

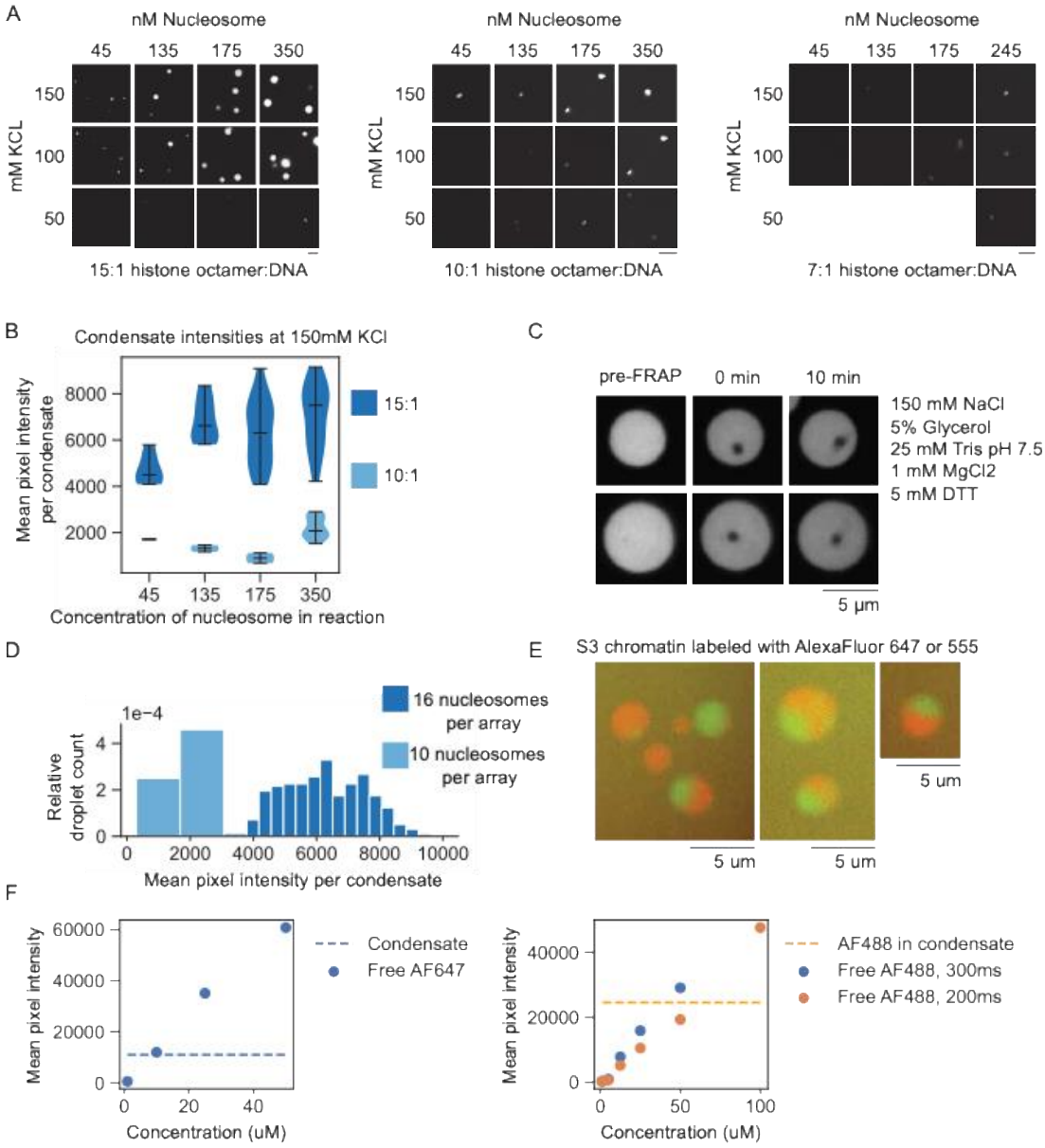

Figure S1. Characterization of chromatin in condensates. (**A**) Phase diagrams for S3 chromatin with varying ratios of histone octamer:DNA. Scale bars are 5 µm. (**B**) Violin plot of mean pixel intensity per condensate for the phase diagrams in A. For 15:1 left to right: 6, 12, 22, 27 condensates were selected. For 10:1 left to right: 1, 2, 2, 26 condensates were selected. (**C**) Confocal images of two example AF647-Cyp3a11(S3) chromatin condensates in the listed buffer conditions. Quantification of recovery shown in Fig S4B. (**D**) Histogram of mean pixel intensity per condensate for the conditions shown in Fig 1B, with histogram bin number equal to 0.1*number of condensates per condition. (**E**) Confocal images from two-color mixing experiment using AF555 and AF647 labeled S3 chromatin. (**F**) Standard curves for AF647 and AF488 using the same exposure time (ms) and laser power as in experimental conditions.

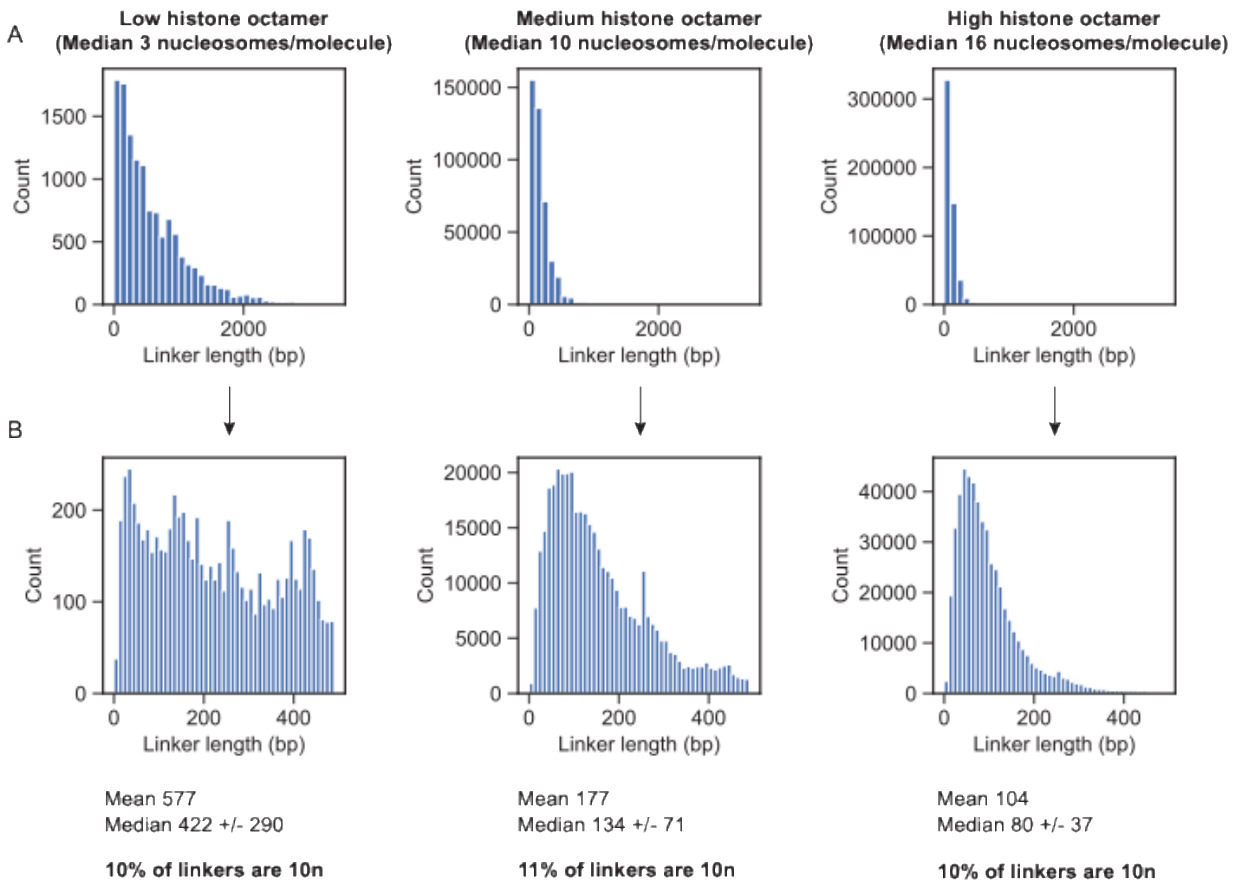

Figure S2. Linker length does not determine chromatin phase separation for S3 chromatin. (**A**) Linker lengths between footprints for three different chromatin assemblies that vary in number of nucleosomes per DNA molecule. Bin size is 100. (**B**) Zoom in of A on footprints 0-500 base pairs in length. Bin size is 10. Mean, median, and median absolute deviation are reported for each condition using all distances.

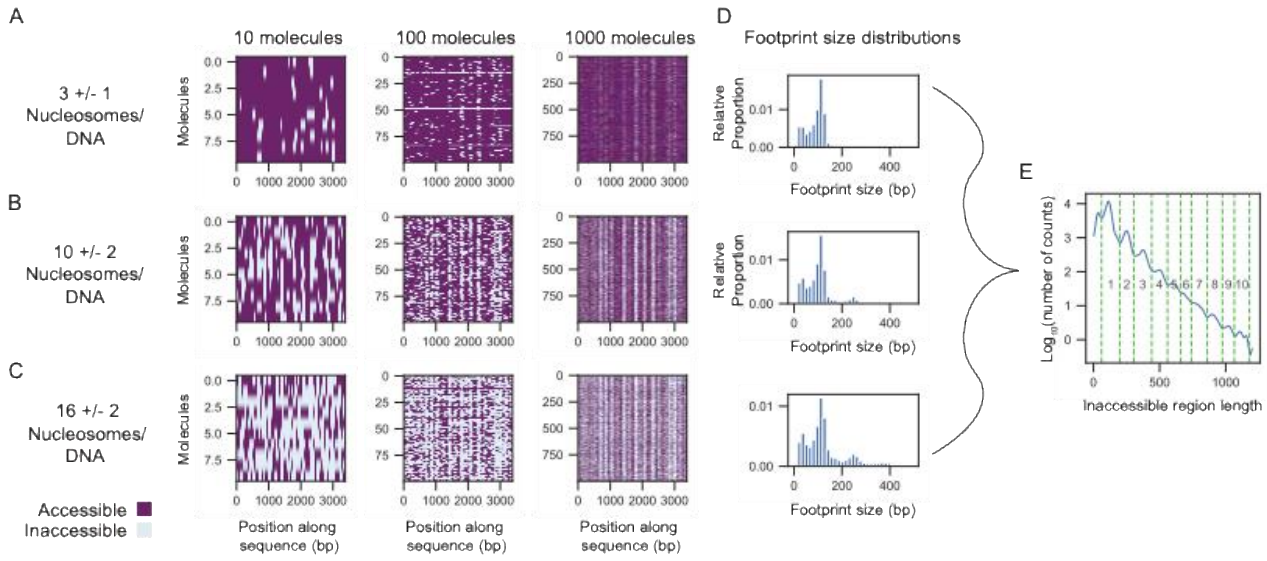

Figure S3. SAMOSA heatmaps at different scales and footprint size distributions. (**A**) Heatmaps of accessible and inaccessible bases for 10, 100, or 1000 molecules for chromatin with median 3 nucleosomes per molecule and MAD of 1. Each row in the heatmap represents a chromatin molecule. (**B**) Same as A for chromatin with median 10 nucleosomes per molecule, MAD of 2. (**C**) Same as A for chromatin with median 16 nucleosomes per molecule and MAD of 2. (**D**) Inaccessible footprint size distributions for chromatin from A-C. Bin size is 15 base pairs. (**E**) Footprints from D were pooled and cutoffs were defined to delineate between the number of estimated nucleosomes within an inaccessible region. Green dashed lines show the cutoffs, and the numbers below indicate the number of nucleosomes that sized region is counted as.

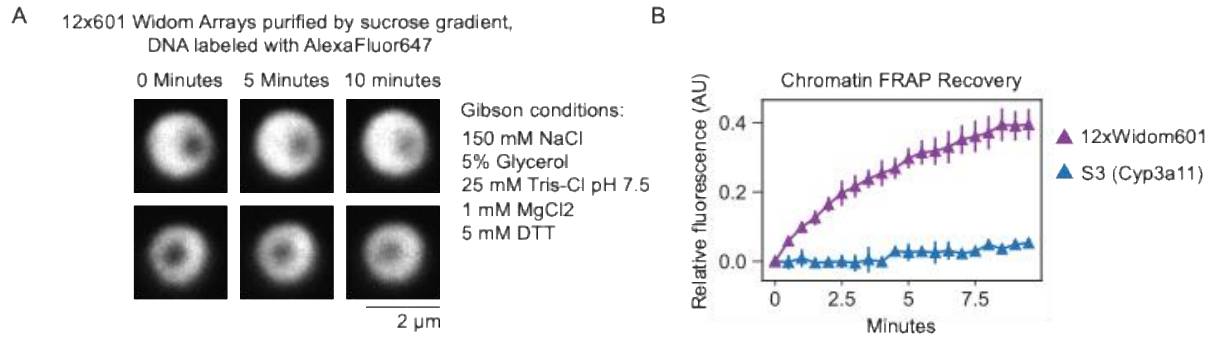

Figure S4. Repetitive chromatin arrays recover from photobleaching. (**A**) Confocal images of two example 12xWidom601 chromatin condensates labeled with AF647 before and after photobleaching in the listed buffer. (**B**) Quantification of recovery after photobleaching for the 12xWidom601 chromatin in A, n=5 droplets, and the S3 chromatin in Fig S1C, n=2 droplets. Recovery is normalized to prebleached droplet intensity and unbleached droplets over the time course.

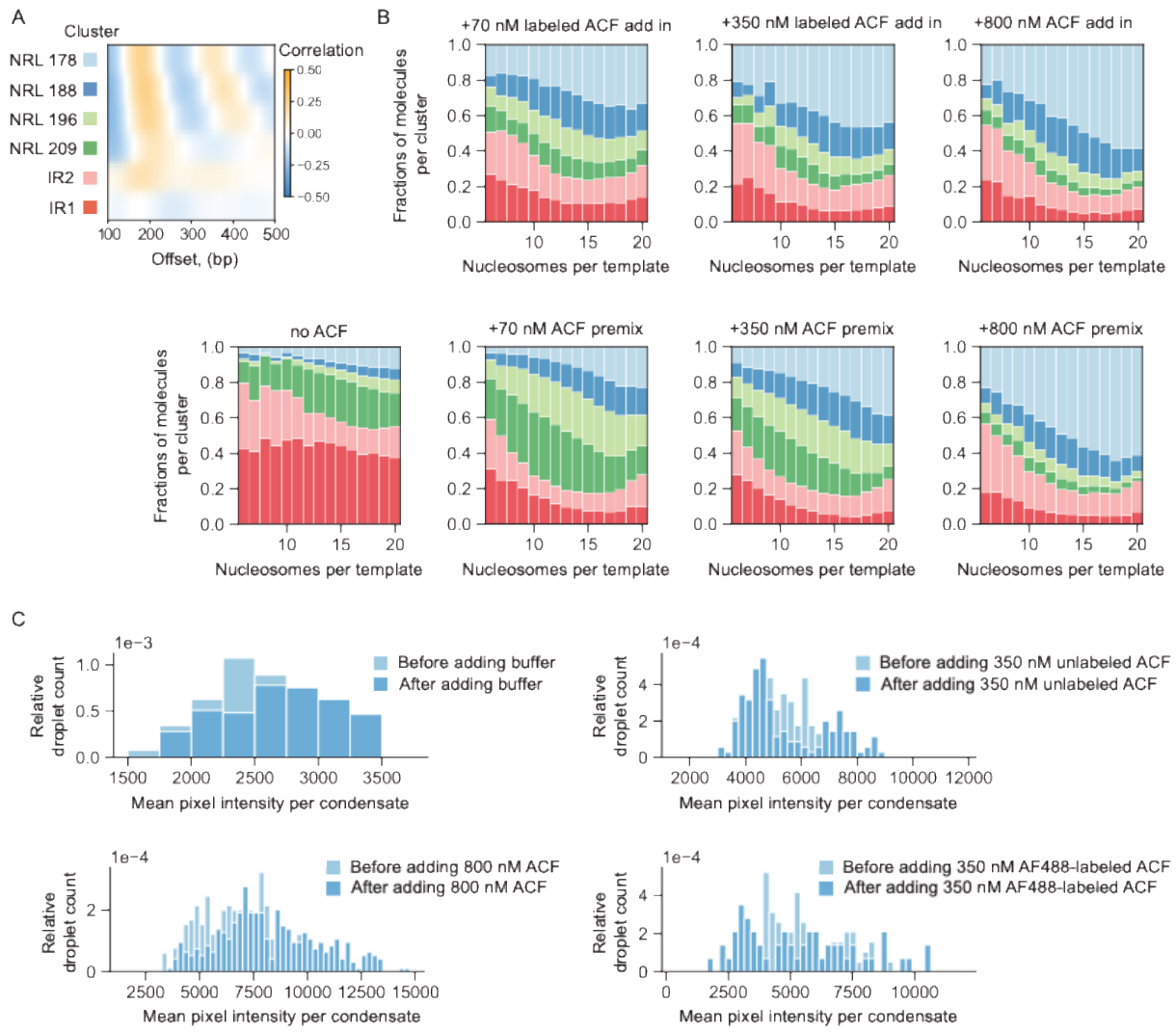

Figure S5. ACF is a density dependent remodeler within chromatin condensates and addition of ACF to condensates does not affect condensate intensity. (**A**) Average single-molecule autocorrelograms resulting from Leiden clustering of individual molecules. This is identical to the plot in Fig 4, as all RSC samples and ACF samples were clustered together. (**B**) Average single-molecule autocorrelograms following Leiden clustering of individual molecules as shown in Fig 4. All samples were clustered together. (**C**) Histograms of mean pixel intensity per condensate before and after ACF add-ins, with histogram bin number equal to 0.1*number of condensates per condition.

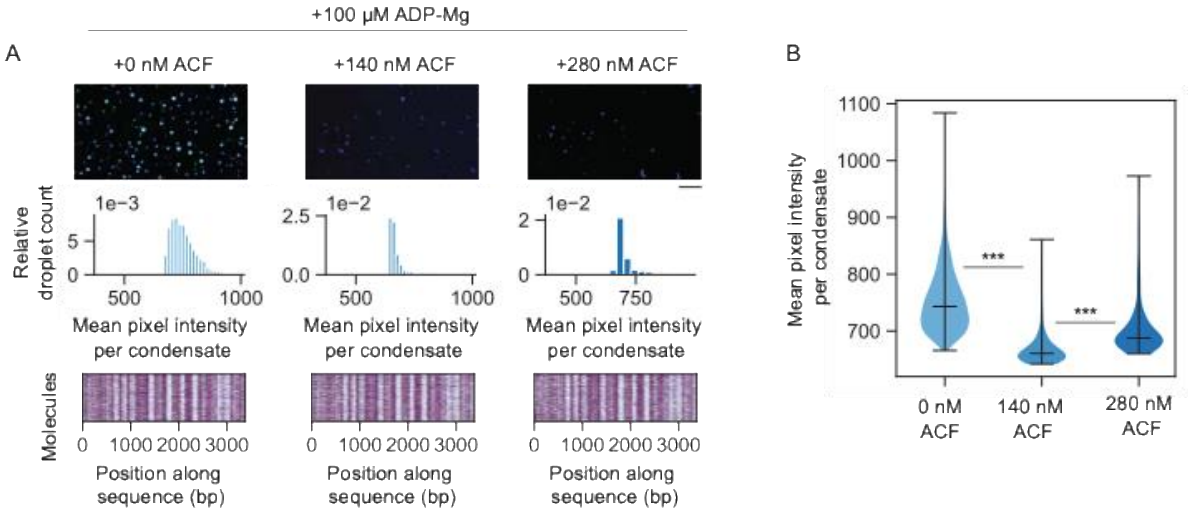

Figure S6. ACF inhibits condensate formation in the presence of ADP. (**A**) Widefield images showing Alexa647 fluorescence. Initial chromatin array concentration in reaction is 20 nM, 260 nM nucleosome. Scale bar is 20 µm. Histograms of mean pixel intensity per condensate with histogram bin number equal to 0.1*number of condensates per condition. Left to right: 3124, 392, and 203 condensates were selected. Heatmaps show accessible and inaccessible bases for 1000 molecules per condition. (**B**) Violin plot of mean pixel per droplet intensities from A.

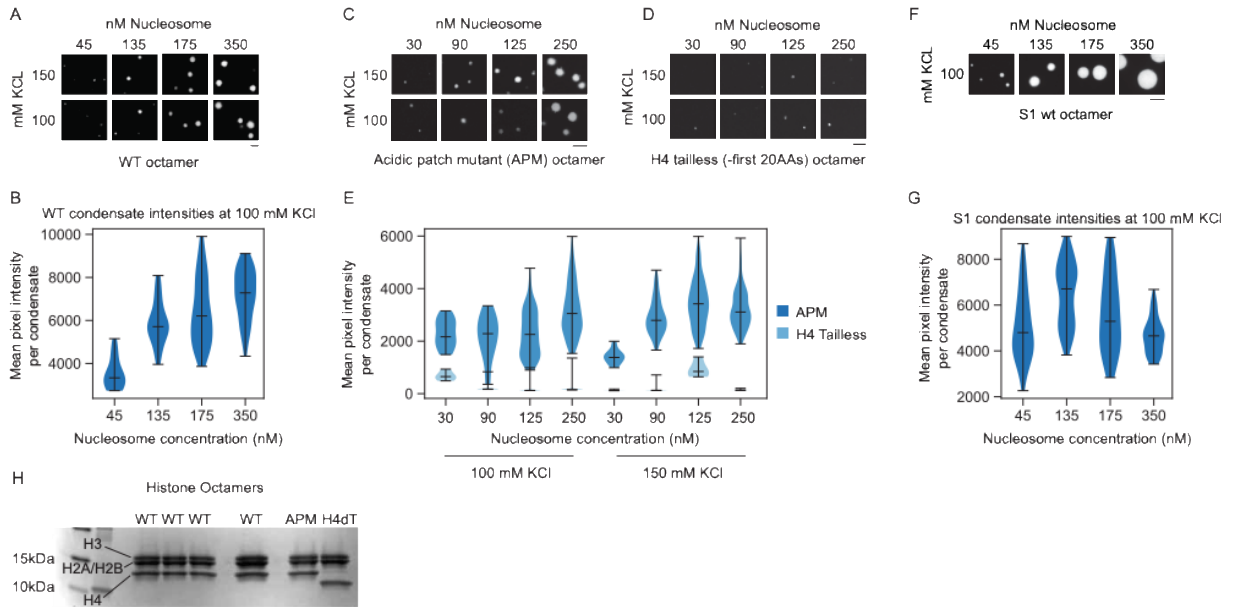

Figure S7. Characterization of S3 chromatin with mutant histone octamer and S1 chromatin with WT octamer. (**A**) Phase diagram for WT S3 chromatin, data repeated from Figure S1. (**B**) Violin plot of mean pixel intensity per condensate for the 100 mM KCl row of the phase diagram in A. (**C**) Phase diagram for acidic patch mutant histone octamer chromatin. (**D**) Phase diagram for H4 tailless histone octamer chromatin. (**E**) Violin plot of mean pixel intensity per condensate for the phase diagrams in C and D. APM left to right: 13, 18, 208, 409, 15, 147, 185, 303 condensates were selected. H4 tailless left to right: 4, 222, 527, 342, 1131, 619, 4, and 769 condensates were selected. (**F**) Phase diagram for WT S1 chromatin assembled with 14:1 histone octamer:DNA. The S1 sequence used here is ~2200 base pairs. All scale bars are 5 μm. (**G**) Violin plot of mean pixel intensity per condensate for the phase diagram in F at 100 mM KCl. Left to right: 172, 126, 61, 64 condensates were selected. (**H**) Validation of histone octamers.

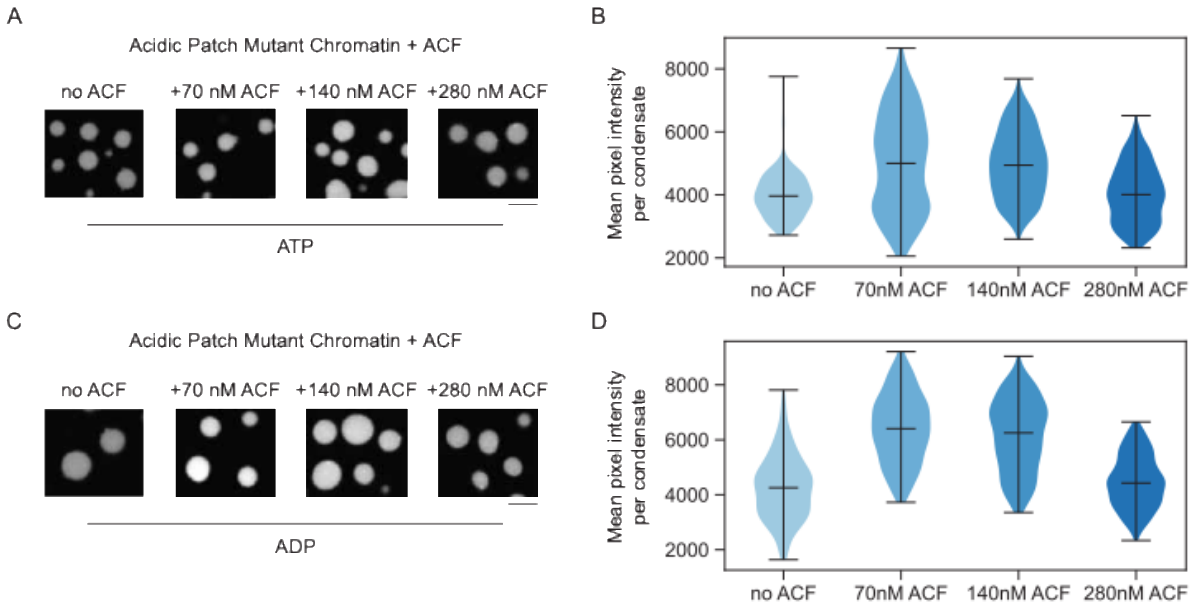

Figure S8. Acidic patch chromatin condensation is not inhibited by ACF. (**A**) APM chromatin condensates with increasing ACF in the presence of 100 μM ATP-Mg. Reaction scheme is outlined in Figure 2 and chromatin array is 20 nM. (**B**) Violin plot of mean pixel intensity per condensate for the reactions in A. Left to right: 264, 709, 1441, 1316 condensates were selected. (**C**) APM chromatin condensates with increasing ACF in the presence of 100 μM ADP. Chromatin array is 20 nM. (**D**) Violin plot of mean pixel intensity per condensate for the reactions in C. Left to right: 362, 442, 776, 988 condensates were selected.

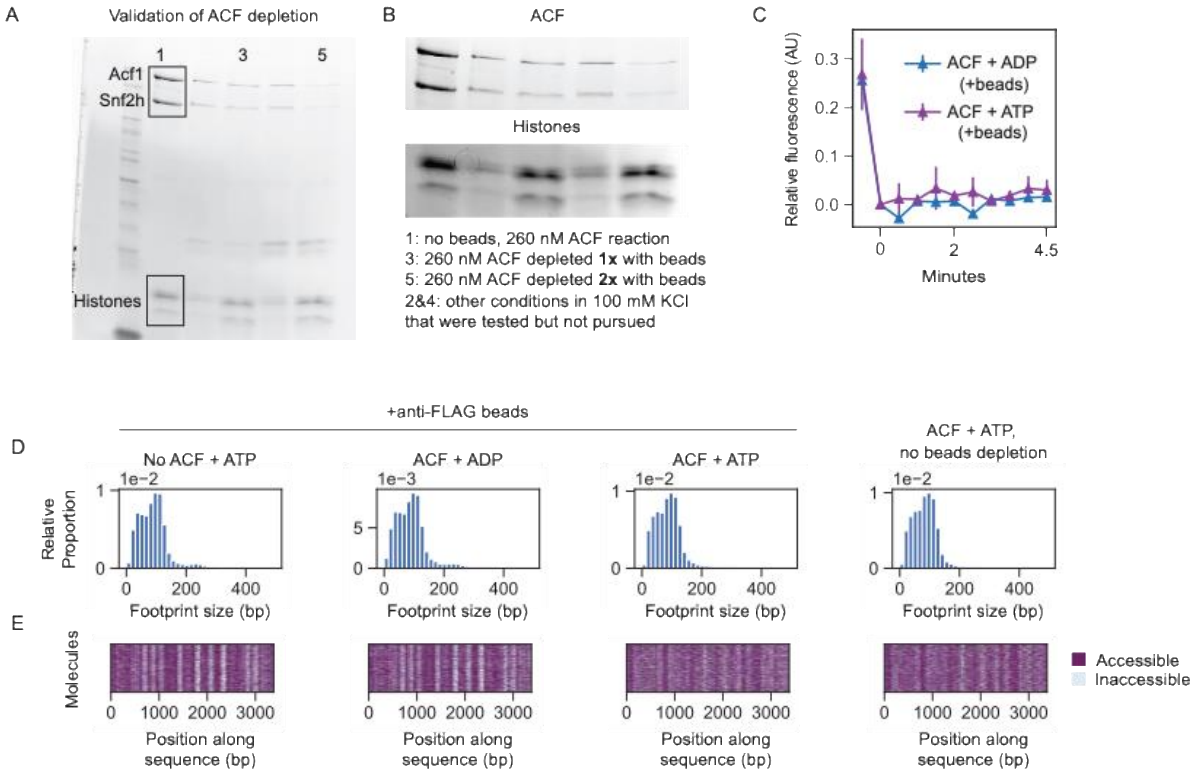

Figure S9. Depleting ACF from chromatin via FLAG-beads. (**A**) SDS-PAGE gel showing amount of ACF and histones left in reactions after 0x, 1x, or 2x incubation with FLAG beads. (**B**) Same gel as A, lanes 1-5, with contrast adjusted to show depletion of ACF and retention of histones. Molar ratio of ACF/histone for lane 1 is 1.03, for lane 3 is 0.09, and for lane 5 is 0.03. (**C**) Quantification of recovery after photobleaching for S3 condensates after ACF depletion, n=3 for ATP and n=1 for ADP. Recovery is normalized to intensity of unbleached droplets over the time course. (**D**) Inaccessible footprint size distributions. Bin size is 15 base pairs. (**E**) Heatmaps of accessible and inaccessible bases. 1000 molecules are shown per condition.

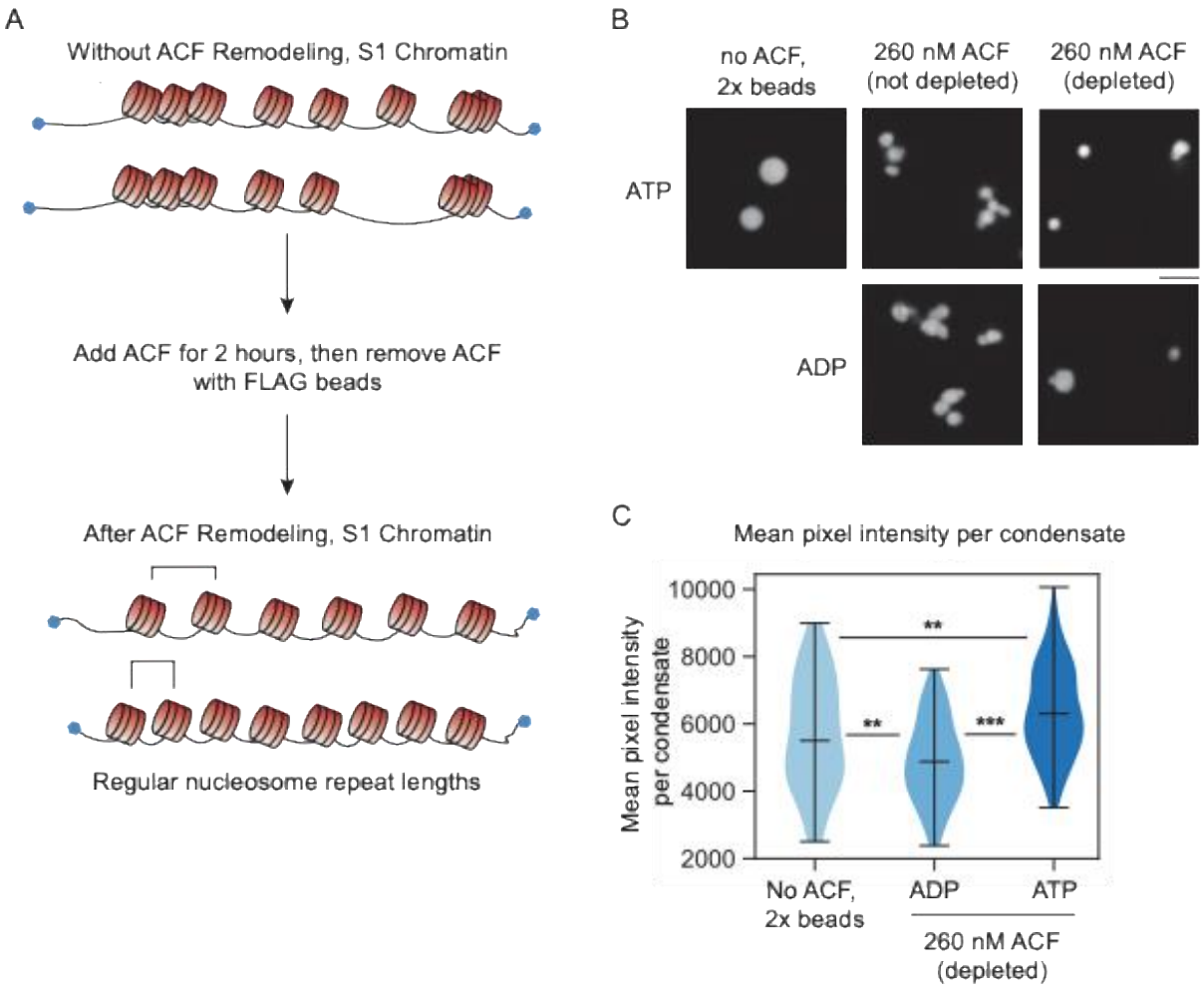

Figure S10. Depleting ACF from S1 chromatin. (**A**) Reaction scheme for ACF depletion experiment. (**B**) Condensates with or without ACF depletion. Scale bar is 5 μm. (**C**) Violin plot of mean pixel intensity per condensate for reactions after ACF depletion. Left to right: 50, 74, 183 condensates were selected.

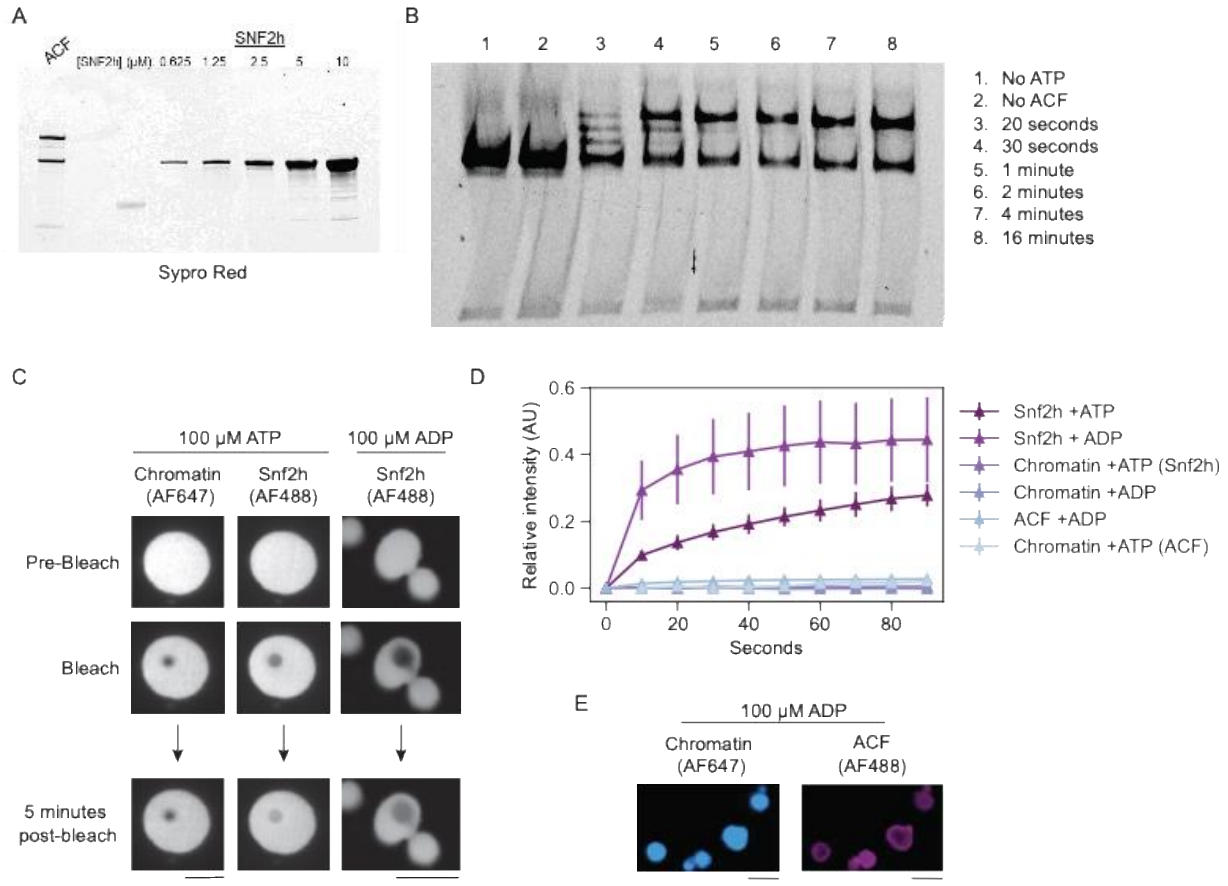

Figure S11. Snf2h recovers from photobleaching and uniformly distributes through chromatin condensates. (**A**) Quantification gel of ACF using Snf2h standards. (**B**) Validation that ACF centers end-positioned 0-60 Widom601 mono-nucleosomes. (**C**) Confocal images of AF647 and AF488 fluorescence in various add-in conditions. Fluorescence intensity is not normalized across columns. (**D**) Quantification of recovery after photobleaching for same conditions as in C along with additional conditions, n=3-5 droplets per condition. Recovery is normalized to intensity of unbleached droplets over the time course. (**E**) ACF distribution throughout chromatin condensates in conditions with ADP. Chromatin array is initially 30 nM. Scale bars are 5 μm.

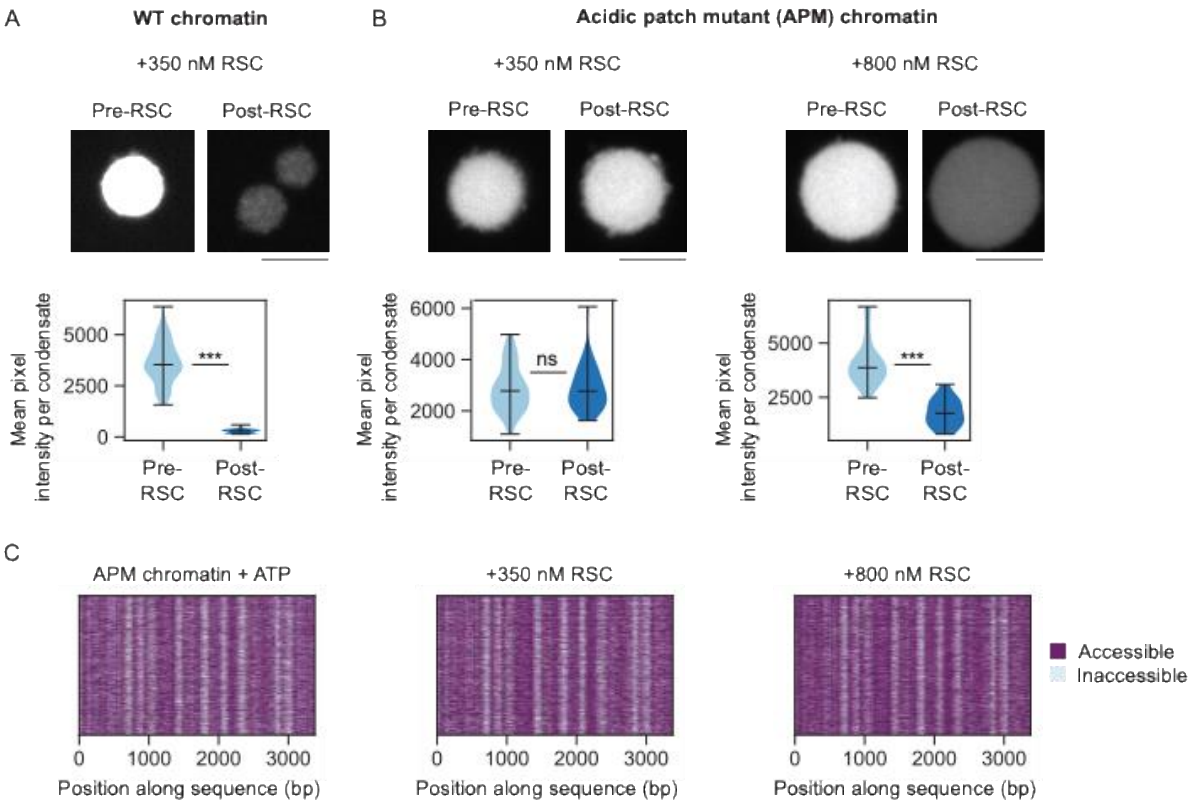

Fig S12: RSC decondenses APM chromatin more modestly than WT chromatin. (**A**) WT chromatin condensates before and after adding 350 nM RSC at 100 μM ATP-Mg and 300 nM nucleosome. Violin plot shows mean pixel intensity per condensate for the reactions above. Left to right: 274, 318 condensates were selected. (**B**) APM chromatin condensates before and after adding 350 nM or 800 nM RSC at 100 μM ATP-Mg and 300 nM nucleosome. Violin plot shows mean pixel intensity per condensate for the reactions above. Left to right: 64, 53, 79, 27 condensates were selected. All scale bars are 5 μm. (**C**) Heatmaps of accessible and inaccessible bases for APM chromatin with or without 350 nM or 800 nM RSC in the presence of 100 μM ATP-Mg (same reactions as in B). 2000 molecules are shown for each condition.

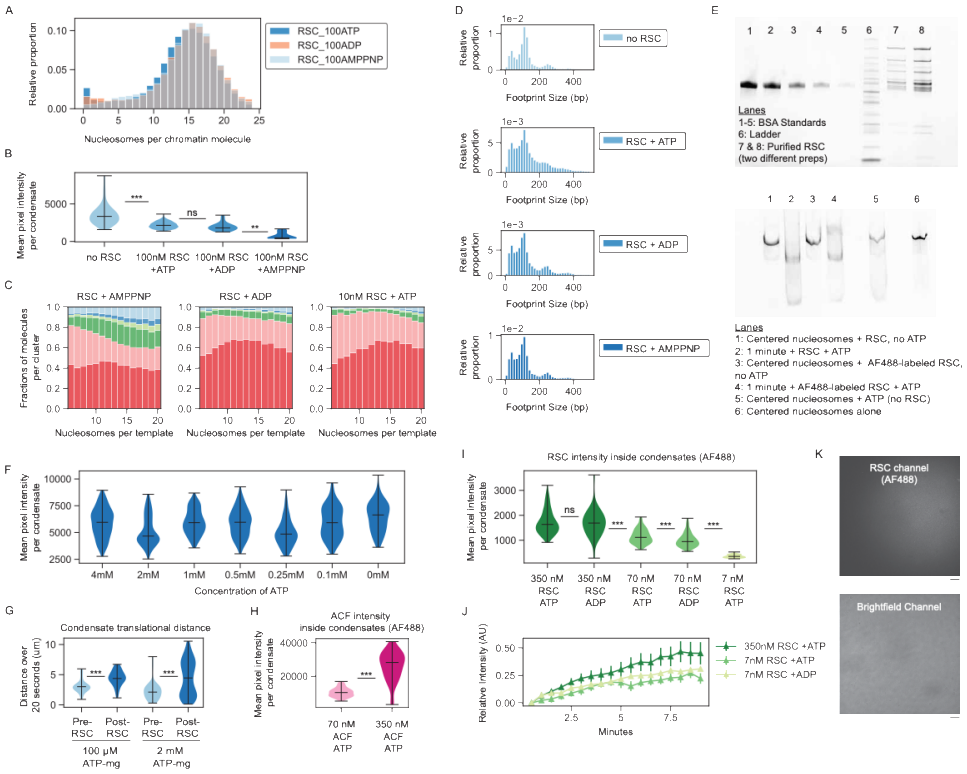

Figure S13. Effects of RSC remodeling on chromatin. (**A**) Histogram of nucleosomes per chromatin molecule for each condition with RSC in Figure 4. (**B**) Violin plot of mean pixel intensity per condensate (AF647 channel) for conditions in Figure 4. Left to right: 178, 768, 17, 15 condensates were selected. (**C**) Stacked bar chart representation of cluster representation in Fig 4, plotted as a function of nucleosome density. (**D**) Inaccessible footprint size distributions for chromatin from conditions in Figure 4. Bin size is 15 base pairs. (**E**) Top gel is quantification gel of RSC using BSA standards. Bottom gel is validation that labeled and unlabeled RSC remodel centered 40-40 Widom601 mono-nucleosomes. (**F**) Violin plot of mean pixel intensity per condensate for a titration of ATP-mg with S3 chromatin at 260 nM nucleosome and 1.5 mM free Mg^{2+}. Reactions were incubated in the phasing plate overnight before imaging. Left to right: 287, 392, 143, 358, 504, 199, and 92 condensates were selected. (**G**) Violin plot of size-matched condensate distance before and after RSC add-in as shown in Fig 5F, but with no minimum cutoff for condensate distance. Left to right: 78, 30, 43, and 209 condensates were selected. (**H**) Violin plot of mean pixel intensity per condensate (AF488 channel) after adding labeled ACF into reactions as shown in Figure 3E. Left to right: 101, 73 condensates were selected. (**I**) Violin plot of mean pixel intensity per condensate (AF488 channel) after adding labeled RSC into reactions as shown in Figure 5G. Left to right: 449, 44, 96, 137, 111 condensates were selected. (**J**) Quantification of AF488 (RSC) recovery after photobleaching for the condensates in Figure 5G along with additional conditions, n=3-6 droplets per condition. Recovery is normalized to prebleached droplet intensity and unbleached droplets over the time course. (**K**) 350 nM RSC (labeled with AF488) does not form condensates in the absence of chromatin. Scale bars are 10 µm.

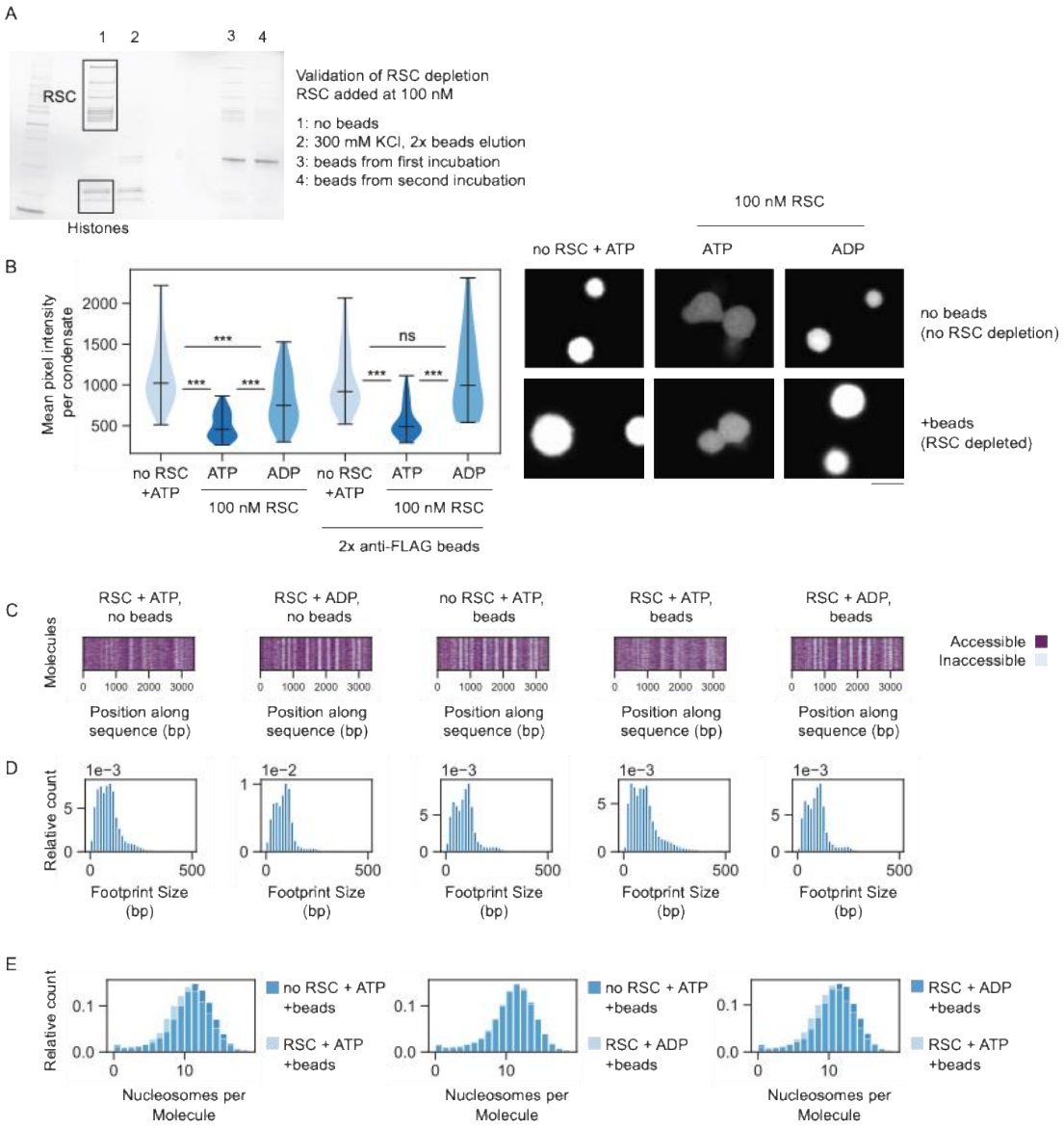

Figure S14. RSC-remodeled chromatin forms condensates with lower chromatin density and irregular footprint size even after depletion of 100 nM RSC. (**A**) Validation of RSC depletion with FLAG beads. In lanes 3 and 4, FLAG beads were boiled in SDS dye after incubation. After boiling, the supernatant was run to determine what bound to the beads. (**B**) Violin plot of mean pixel intensity per condensate and corresponding images from the RSC depletion experiment before and after RSC depletion. Left to right: 88, 52, 36, 65, 67, 34 condensates were selected. Chromatin array was added to remodeling reactions at 20 nM. Scale bar is 5 μm. (**C**) Heatmaps of accessible and inaccessible bases for conditions in the RSC depletion experiment. 1000 molecules are shown for each condition. (**D**) Inaccessible footprint size distributions for RSC depletion experiment. Bin size is 15 base pairs. (E) Histograms of nucleosomes per molecule for conditions in this experiment.

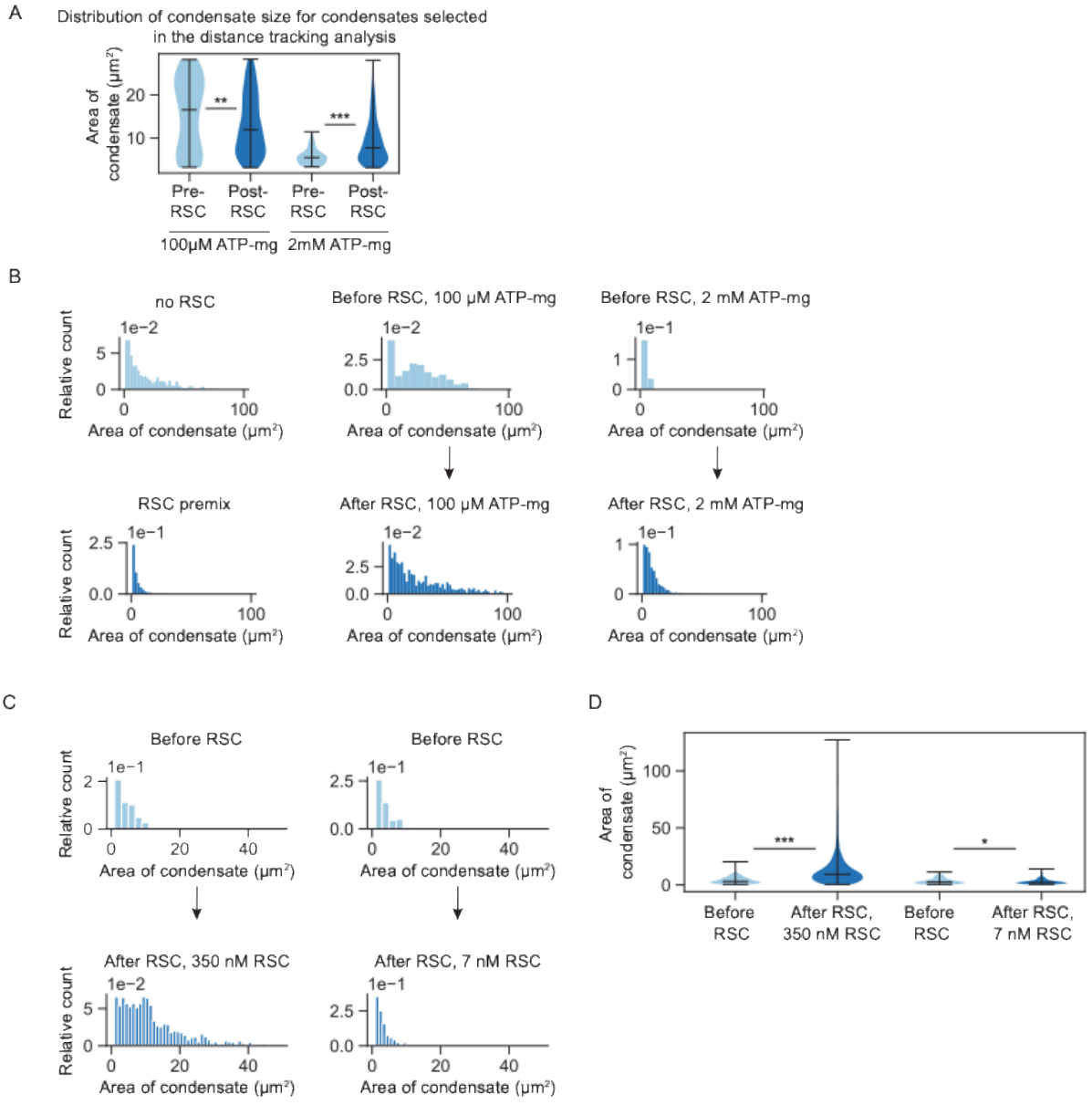

Figure S15. Effects of RSC on condensate area and distance. (**A**) Violin plots of condensate area in each RSC condition in Figure 5 for condensates 2-6 μm in diameter that were used for the size matched translational distance analysis in Figure 5. (**B**) Histograms of condensate area before and after RSC add-in, with histogram bin number equal to 0.1*number of condensates per condition. (**C**) Histogram of condensate area before and after AlexaFluor-488 labeled RSC add-in, with histogram bin number equal to 0.1*number of condensates per condition. (**D**) Violin plot of condensate area in each condition with AlexaFluor-488 labeled RSC in Figure 5.

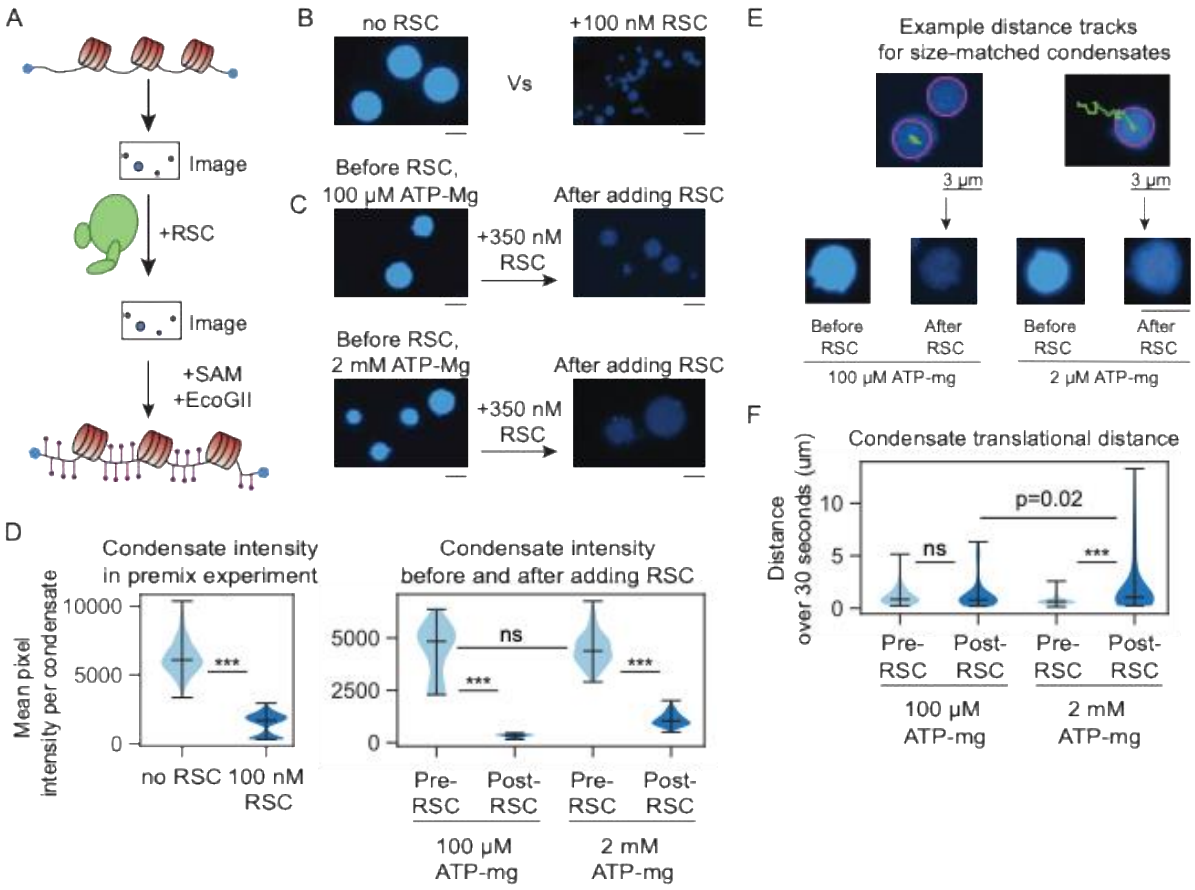

Fig S16: RSC decondenses chromatin condensates and increases condensate motion in an ATP-dependent manner when condensate intensities in high and low ATP conditions are matched before RSC add in. (**A**) Scheme of RSC add-in experimental workflow. (**B**) Confocal images of chromatin condensates for the RSC premix experiment (data repeated from Fig 5B) in conditions with 220 nM nucleosome, 100 μM ATP-Mg. Estimated mean nucleosome concentration inside condensates is 38 uM (control reaction) and 9 μM (+100 nM RSC reaction). (**C**) RSC add-in experiment as shown in A, done in conditions with either 100 μM ATP-Mg or 2 mM ATP-Mg and 300 nM nucleosome. Estimated mean nucleosome concentration inside condensates is 21 μM (before RSC, 100 μM ATP-mg), 2 μM (after RSC, 100 μM ATP-mg), 22 μM (before RSC, 2 mM ATP-mg), 6 μM (after RSC, 2 mM ATP-mg). (**D**) Violin plots of mean condensate intensity for premix (left, repeated from Fig 5D) and add in experiments in A and B (right) for condensates 2-4 μm in diameter. For add in experiment left to right: 48, 95, 244, 276 condensates were selected. (**E**) Example traces of condensate xy translational distance over 30 seconds. Distance tracking analysis was limited to condensates with diameter of approximately 3 μm. (**F**) Violin plot of size-matched condensate distance before and after RSC add-in. Left to right: 56, 57, 137, 116 condensates were selected.

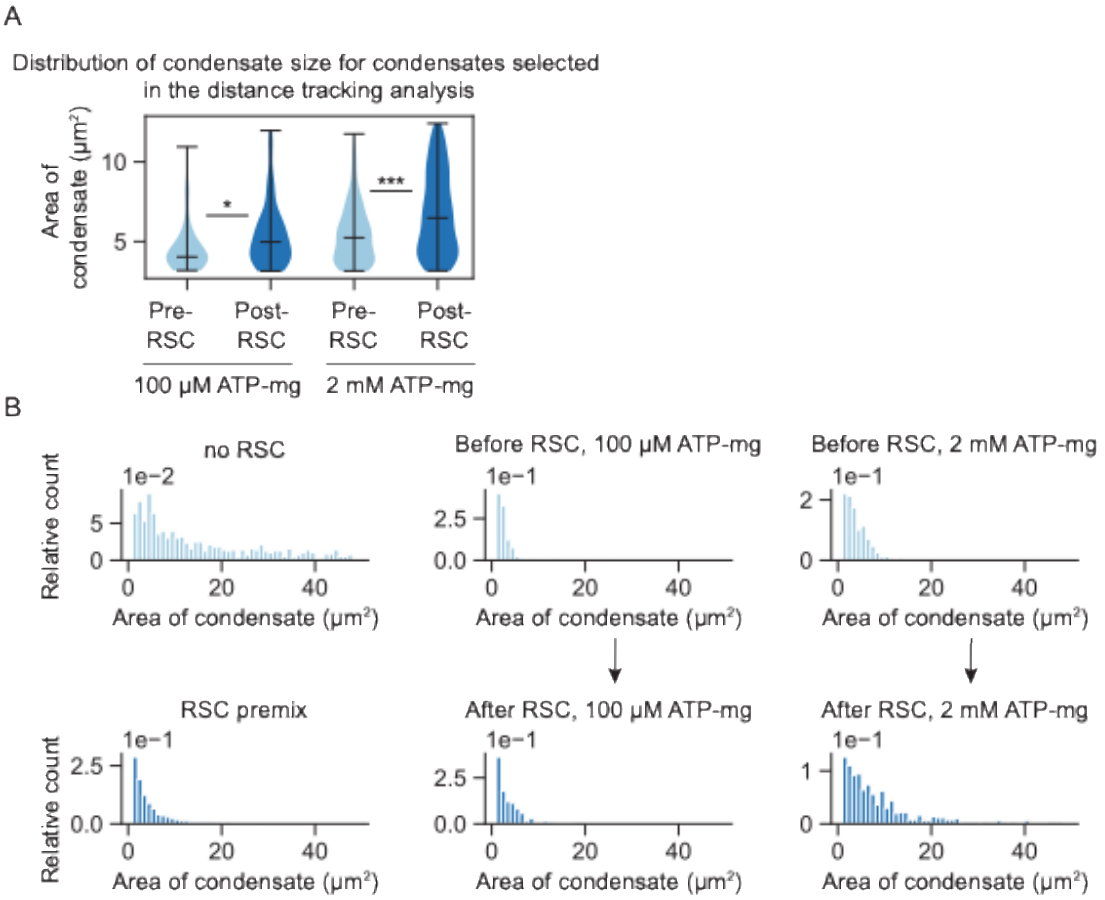

Figure S17. Effects of RSC on condensate area and distance when condensate intensities in high and low ATP conditions are matched before RSC add in. (**A**) Violin plots of condensate area in each RSC condition in Figure S16 for condensates 2-4 μm in diameter that were used for the size matched translational motion analysis in Figure S16. (**B**) Histograms of condensate area before and after RSC add-in, with histogram bin number equal to 0.1*number of condensates per condition. 'No RSC' and 'RSC premix' conditions are repeated from Figure S15 for comparison to new add-in data.

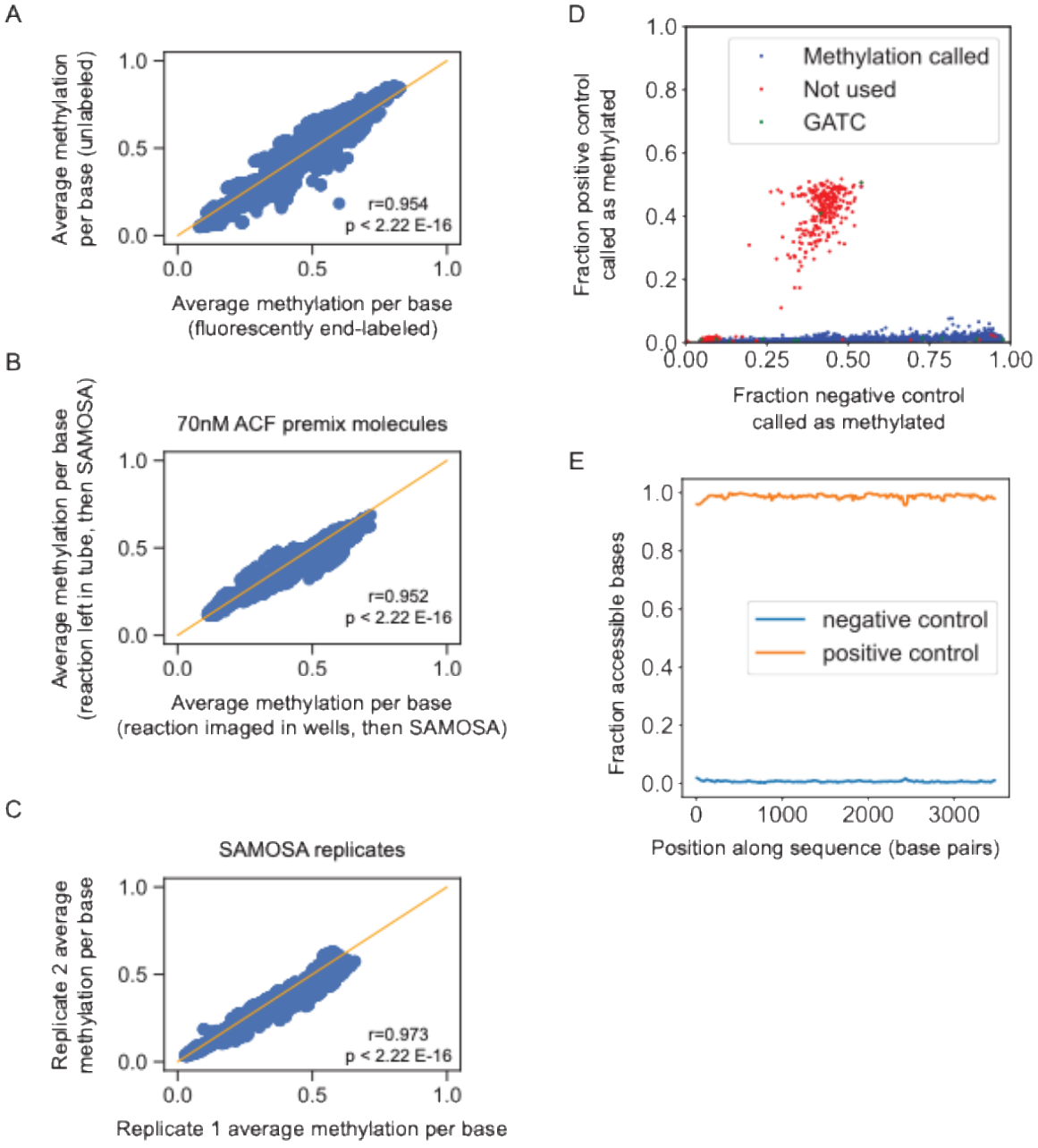

Figure S18. SAMOSA quality control validation. Correlation of average methylation per base for (**A**) unlabeled chromatin and AF647-labeled chromatin, (**B**) chromatin left in tubes before SAMOSA and chromatin added to microscopy plate before SAMOSA, (**C**) two replicate SAMOSA experiments. Correlated molecules all have the same number of nucleosomes per molecule. (**D**) Adenine distribution for all adenines on the S3 sequence. (**E**) Average methylation for positive and negative control molecules (S3 DNA fully methylated or unmethylated, respectively).

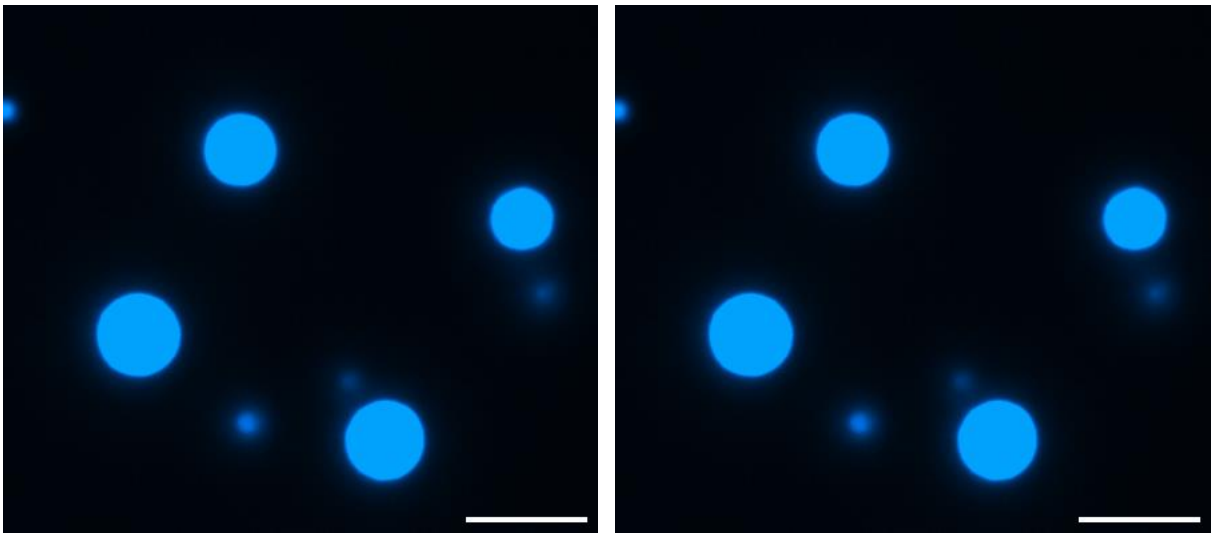

Movie S1 and S2. Premix control condensates, 100 μM ATP-mg. Speed is one fps (left) and five fps (right). Scale bar is 10 μm.

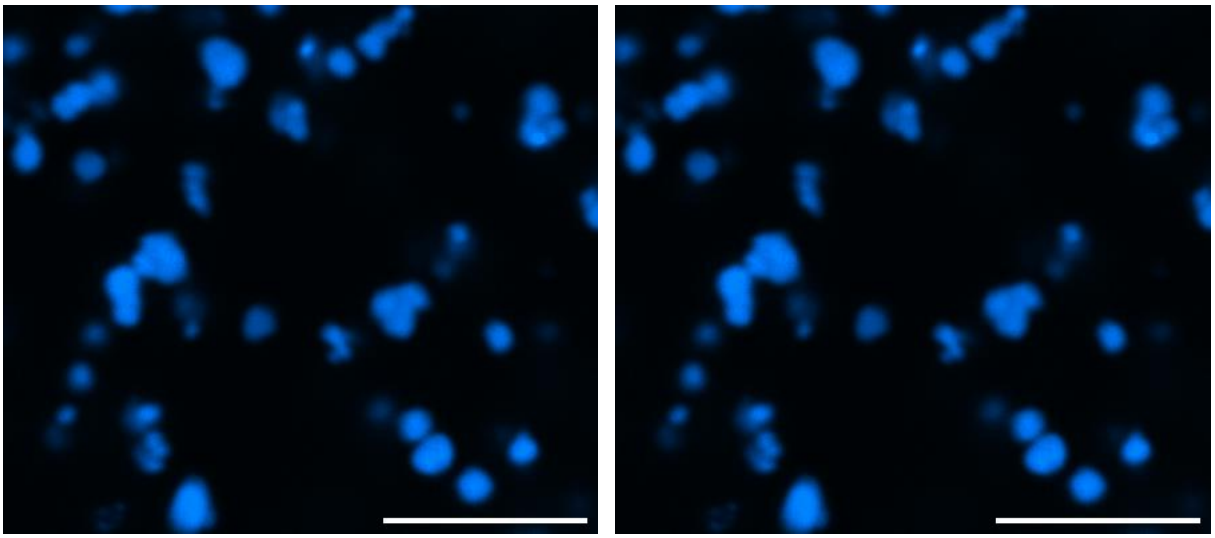

Movie S3 and S4. Premix condensates + RSC, 100 μM ATP-mg. Speed is one fps (left) and five fps (right). Scale bar is 10 μm.

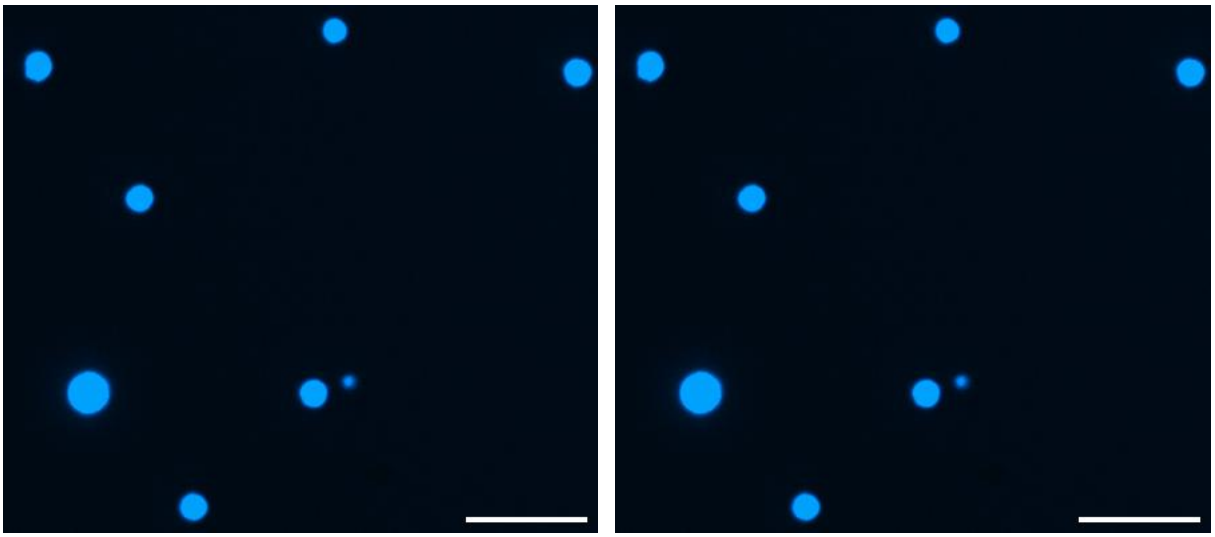

Movie S5 and S6. Before adding RSC to condensates, 2 mM ATP-mg. Speed is one fps (left) and five fps (right). Scale bar is 10 μm.

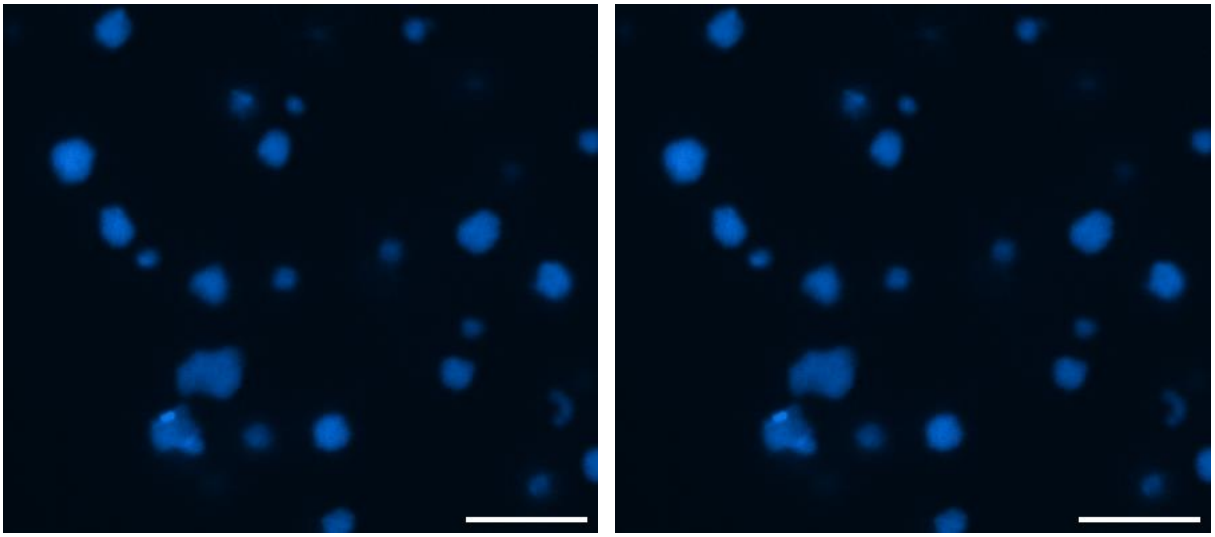

Movie S7 and S8. After adding RSC to condensates, 2 mM ATP-mg + 500 nM RSC. Speed is one fps (left) and five fps (right). Scale bar is 10 μm.

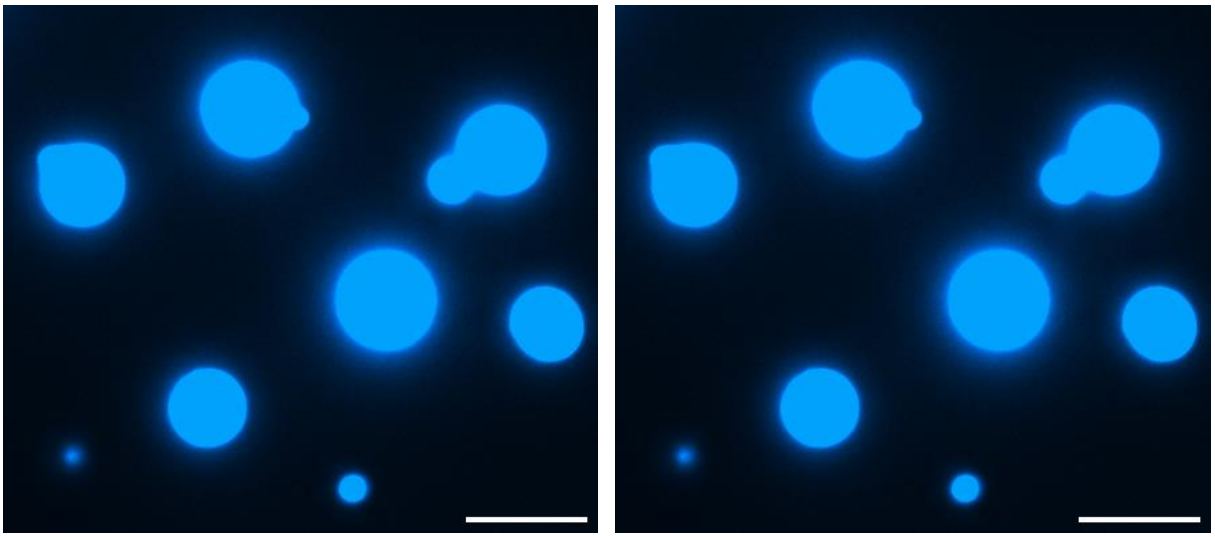

Movie S9 and S10. Before adding RSC to condensates, 100 μM ATP-mg. Speed is one fps (left) and five fps (right). Scale bar is 10 μm.

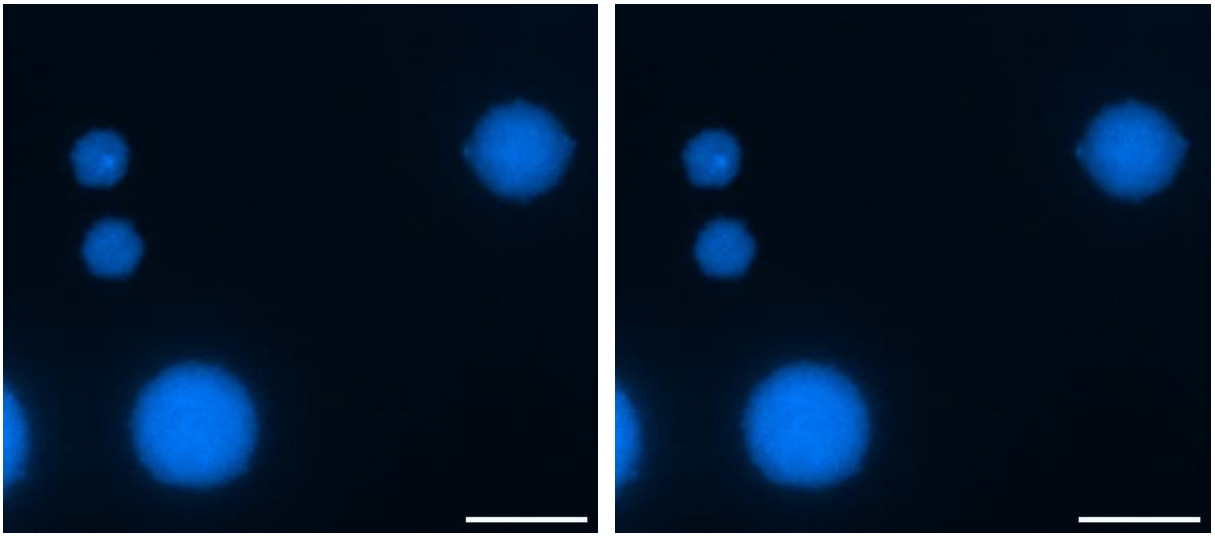

Movie S11 and S12. After adding RSC to condensates, 100 μM ATP-mg + 500 nM RSC. Speed is one fps (left) and five fps (right). Scale bar is 10 μm.